Materials Today Bio 26 (2024) 101085

Contents lists available at ScienceDirect

Materials Today Bio

journal homepage: www.journals.elsevier.com/materials-today-bio

Hyperthermia/glutathione-triggered ferritin nanoparticles amplify the ferroptosis for synergistic tumor therapy

Yiting Chen [a], Xinhong Li [a], Kuankuan Luo [a], Tao Wang [a], Tongyao Liu [a], Enhao Lu [a], Rui Wang [a], Yu Luo [a], Xianyi Sha [a,b,*]

[a] Key Laboratory of Smart Drug Delivery (Ministry of Education), School of Pharmacy, Fudan University, Lane 826, Zhangheng Road, Shanghai, 201203, China
[b] Department of Integrative Oncology, Fudan University Shanghai Cancer Center, 270 Dongan Road, Shanghai, 200030, China

ARTICLE INFO

Keywords:
Photothermal therapy
Ferroptosis
Ferritin
Iron oxide nanoparticles
Glutathione consumption

ABSTRACT

Breast cancer is the most diagnosed malignancy in women globally, and drug resistance is among the major obstacles to effective breast cancer treatment. Emerging evidence indicates that photothermal therapy and ferroptosis are both promising therapeutic techniques for the treatment of drug-resistant breast tumors. In this study, we proposed a thermal/ferroptosis/magnetic resonance imaging (MRI) triple functional nanoparticle (I@P-ss-FRT) in which ferritin, an iron storage material with excellent cellular uptake capacity, was attached via disulfide bonds onto polydopamine coated iron oxide nanoparticle (I@P) as photothermal transduction agent and MRI probe. I@P-ss-FRT converted the near-infrared light (NIR) into localized heat which accelerated the release of ferrous ions from ferritin accomplished by glutathione reduction and subsequently induced ferroptosis. The drug-resistant cancer cell lines exhibited a more significant uptake of I@P-ss-FRT and sensitivity to PTT/ferroptosis compared with normal cancer cell lines. *In vivo*, I@P-ss-FRT plus NIR displayed the best tumor-killing potential with inhibitory rate of 83.46 %, along with a decline in GSH/GPX-4 content and an increase in lipid peroxides generation at tumor sites. Therefore, I@P-ss-FRT can be applied to combat drug-resistant breast cancer.

1. Introduction

Globally, female breast cancer has surpassed lung carcinoma as the primary cause of cancer incidences, accounting for 31 % of all new cancer cases [1,2]. Clinically, chemotherapy is the main therapeutic option for triple-negative breast cancer or early-stage breast cancer [3,4]. However, chemotherapy is associated with drug resistance [5–7]. Therefore, there is an urgent need for innovative therapeutics for drug-resistant breast cancer.

Drug-resistant breast cancer cells exhibit mesenchymal phenotype and stemness properties [8–12]. Notably, high-mesenchymal state cells with high expressions of zinc-finger E-box binding homeobox 1 (ZEB1) are sensitive to the lipid peroxidase pathway [13]. Further, the preferential uptake of iron and ferritin by cancer stem-like cells (CSC) has been reported by Rich et al. [14]. Therefore, we postulated that ferroptosis is a potential therapeutic approach for drug-resistant breast cancer.

Ferroptosis, first proposed in 2012 by Dixon SJ, is a new death mode of cells that is initiated by toxic lipid peroxidation (LPO), with a substantial iron dependence [15,16]. A common approach for inducing ferroptosis is to interfere with iron metabolism by leveraging the degradation property of iron oxide nanoparticles (IONPs), that is, degradation to iron ions after IONPs enter the acidic lysosomal compartments and catalyzation with H_2O_2 to produce hydroxyl radicals via the Fenton reaction [17–19]. The inefficiency of ferroptosis is largely attributed to slow degradation of IONPs, unfavorable catalytic conditions in the tumor microenvironment (TME) away from the ideal pH (2.5–3.5) for Fenton reactions, and the presence of glutathione (GSH)/glutathione peroxidase 4 (GPX-4) pathway, which is responsible for detoxifying LPO to nontoxic lipid alcohols [20–23].

Ferritin, which is made up of an iron mineral core that can store up to 4500 atoms of iron and a protein shell on which the 3-fold hydrophilic channels for Fe^{2+} transport are located, is an essential protein for intracellular iron storage and iron homeostasis [24,25]. Reducing agents, such as GSH, can release soluble Fe^{2+} from the ferritin mineral

* Corresponding author. Key Laboratory of Smart Drug Delivery (Ministry of Education), School of Pharmacy, Fudan University, Lane 826, Zhangheng Road, Shanghai, 201203, China.
E-mail address: shaxy@fudan.edu.cn (X. Sha).

https://doi.org/10.1016/j.mtbio.2024.101085
Received 6 March 2024; Received in revised form 22 April 2024; Accepted 3 May 2024
Available online 4 May 2024

core by crossing the ferritin shell and entering the ferritin interior or by using a particular electron transfer pathway, which is accompanied by consumption of reducing agents [26–30]. Interestingly, hyperthermia can widen ferritin channels or slightly separate ferritin subunits, thereby enhancing the entry of reducing agents into the interior of ferritin [31–33]. The thermal-responsive property of ferritin enlightens us to take advantage of photothermal therapy (PTT), as the increased temperature brought by PTT results in opening of ferritin channels, suppression of GSH, and increased release of ferrous ions, all of which potentiate the effects of ferroptosis. Horse spleen ferritin, which is rich in L chains, can specifically recognize and bind scavenger receptor class A member 5 (SCARA5) that is upregulated in breast tumors, promoting the cellular uptake of ferritin-decorated nanoparticles [34–37]. Therefore, ferritin functions as an excellent link between PTT and ferroptosis for improved drug-resistant cancer therapy.

We designed a biomimetic nanoparticle (I@P-ss-FRT) based on GSH-triggered and PTT-enlarged ferroptosis for synergistic therapy of drug-resistant cancer. In this study, IONP was chosen as its slow and sustained release of ionic iron in acidic environments, photothermal conversion and magnetic resonance imaging (MRI) contrast. The polydopamine (PDA) coating reinforced photothermal effects synergistically with IONP, and offered a favorable reaction platform for further ferritin modification due to its active catechol hydroxyl groups [38–40]. As shown in Fig. 1, due to ferritin-mediated endocytosis, drug-resistant tumor cells exhibited effective uptake of nanoparticles, facilitating intracellular functions, compared with non-resistant cells. Apart from directly suppressing tumor growth, the NIR-mediated hyperthermia triggered ferritin's Fe^{2+} release in GSH rich TME. The rapid and massive iron release from ferritin played co-operative and complementary roles with the slow but continuous iron release from IONP core, maximizing the benefits of Fe^{2+} in ferroptosis. Activation of ferroptosis with enlarged efficiency was accomplished by suppression of intracellular GSH levels and increased ferrous ions accumulation. The mutually beneficial relationship between PTT and ferroptosis, in which photothermal heating of I@P-ss-FRT sparked ferroptosis and ferroptosis that in turn made up for the incomplete ablation by PTT due to heterogeneous heat distribution, presented a strong and synergistic efficacy for inhibiting drug-resistant tumor.

2. Materials and methods

2.1. Materials

Dimercaptosuccinic acid (DMSA)-IONP, black magnetite Fe_3O_4 nanoparticle, was purchased from Nanjing NanoEast Biotech Co., Ltd (Nanjing, China). Horse spleen ferritin was provided by Sigma-Aldrich (St. Louis, USA). Doxorubicin HCl, Tris-HCl buffer (10 mmol/l (mM), pH 8.5), fluorescein isothiocyanate (FITC), phosphate-buffered saline (PBS), human recombinant insulin, recombinant human epidermal growth factor (rh-EGF), recombinant human basic fibroblast growth factor (rh-bFGF), agarose, and cell counting kit-8 (CCK-8) assay were obtained from Dalian Meilun Biotechnology Co., Ltd (Dalian, China). GSH assay kit and MDA assay kit came from Jiancheng Bioengineering Institute (Nanjing, China). Cell lysis buffer, phenylmethanesulfonylfluoride (PMSF), SDS-PAGE sample loading buffer, nonfat powdered milk, HRP-labeled goat anti-mouse IgG (H + L), HRP-labeled goat anti-rabbit IgG (H + L), BeyoECL Plus, BCA protein assay kit, Calcein/PI cell viability/cytotoxicity assay kit, reactive oxygen species (ROS) assay kit, mannose receptor C-type 1 (MRC1) rabbit polyclonal antibody and β-actin mouse monoclonal antibody were

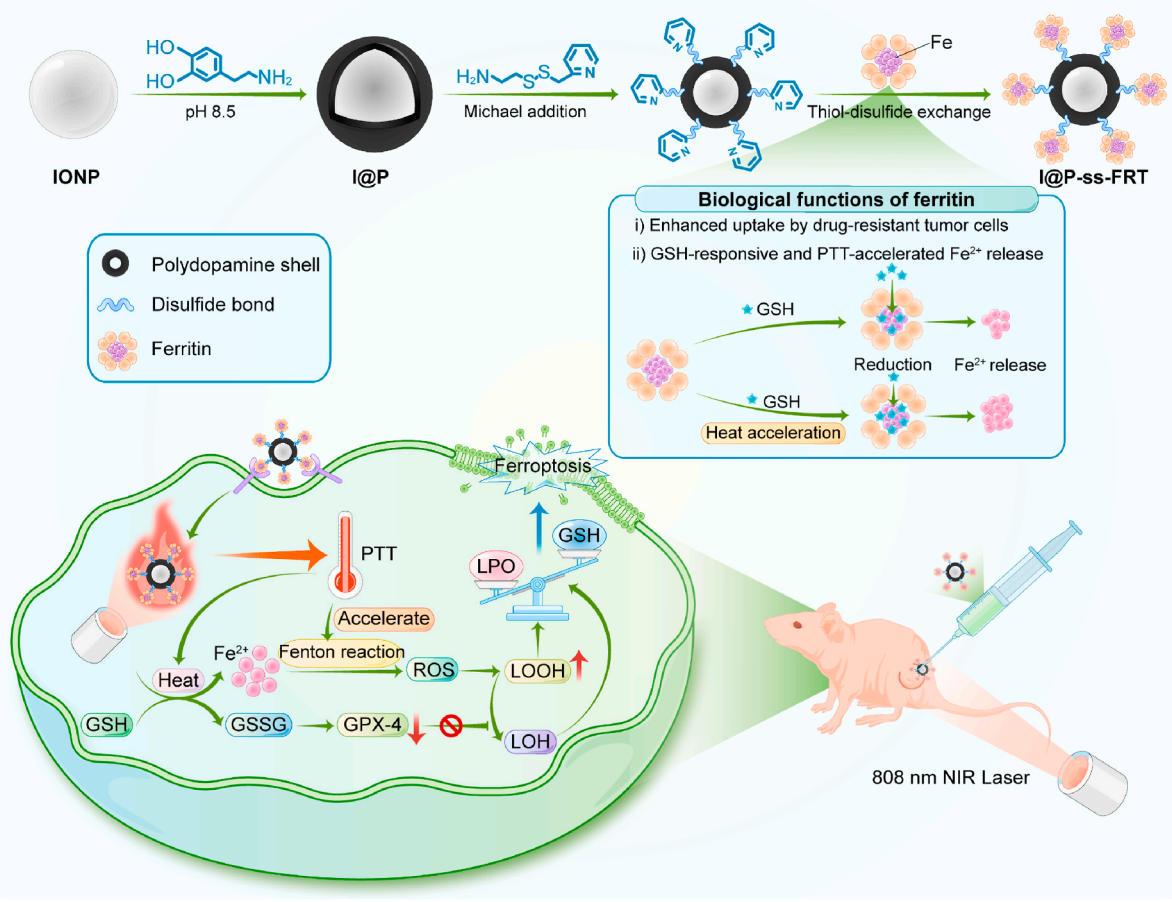

Fig. 1. Schematic illustration of the structure of I@P-ss-FRT, ferritin functions, and mechanisms of PTT-enhanced ferroptosis.

bought from Beyotime Biotechnology Co., Ltd (Shanghai, China). Ammonia water (28–30 %) and acetone were obtained from Sinopharm Chemical Reagent Co., Ltd (Shanghai, China). GSH, 1,10-Phenanthroline, and dopamine hydrochloride were supplied by Aladdin Biochemical Technology Co., Ltd (Shanghai, China). Deferoxamine methane sulfonate (DFOM) was obtained from J&K Scientific (Beijing, China). Z-VAD-fmk was obtained from Bidepharm (shanghai, China). Pyridyl disulfide cysteamine·HCl was bought from Shanghai Acmec Biochemical Co., Ltd (Shanghai, China). FerroOrange probe was purchased from DOJINDO Laboratories (Japan). B-27™ Supplement (50 ×), BODIPY™ $^{581/591}$ C11, and CD206 monoclonal antibody (MR6F3) were obtained from Thermo Fisher Scientific Inc (MA, USA). Hematoxylin-eosin (H&E) staining kit and 5,5′,6,6′-tetrachloro-1,1′,3,3′-tetraethylimidacarbocyanine (JC-1) assay kit were bought from Beijing Solarbio Science & Technology Co., Ltd. (Beijing, China). Murine interferon-γ (IFN-γ) and lipopolysaccharide (LPS) were purchased from PeproTech Inc (NJ, USA). Anti-ferritin light chain antibody (EPR5260) and GPX-4 antibody (EPNCIR144) were bought from Abcam (Cambridge, UK).

2.2. Cell lines

MCF-7 (a human breast cancer cell line), RAW 264.7 (murine macrophages), L929 (a mouse fibroblast cell line), and 4T1 (mouse mammary carcinoma cells) were purchased from the Cell Bank of the Chinese Academy of Sciences (Shanghai, China). A doxorubicin (DOX)-resistant subline of the MCF-7 cells (*i.e.*, MCF-7/ADR) was obtained from MEIXUAN Biological Science and Technology Ltd (Shanghai, China). Dulbecco's Modified Eagle's Medium (DMEM/high glucose) cell culture medium, Roswell Park Memorial Institute (RPMI-1640), fetal bovine serum (FBS), 0.25 % trypsin-EDTA and penicillin/streptomycin stock solutions were all supplied by Invitrogen Co., Ltd (Carlsbad, USA). MCF-7 cells, RAW 264.7 cells, L929 cells, and 4T1 cells were cultured in DMEM/high glucose with 10 % (v/v) FBS, 100 U/mL penicillin and 0.1 mg/mL streptomycin. MCF-7/ADR cells were treated with RPMI-1640 containing 0.5 μg/mL DOX, 10 % FBS, 100 U/mL penicillin and 0.1 mg/mL streptomycin. All cells were incubated in a humidified incubator with 5 % CO_2 in the air at 37 °C.

2.3. Preparation of polydopamine-coated IONPs (I@P)

As reported previously, PDA coating was deposited on the surface of IONPs by self-polymerization of dopamine in a weak alkaline environment [39,41]. More specifically, 40 mL of pH 8.5 Tris buffer was used to dissolve 1 mg DMSA-IONP and 20 mg of dopamine. This process took place at room temperature for 12 h with mechanical stirring. The I@P was collected by centrifugation and then redispersed in water for future usage.

2.4. Conjugation of ferritin to I@P via disulfide bonds

The obtained I@P was resuspended in Tris buffer containing 25 mg pyridyl disulfide cysteamine·HCl. The solution reacted for 12 h at room temperature with mechanical stirring to produce pyridyl disulfide-I@P via Michael-Type addition, followed by centrifugation to obtain the modified I@P.

Commercial ferritin was further purified for buffer exchange into PBS using a Sephadex G-25S desalting column (HiTrap Desalting 5 mL, Sephadex G-25S, GE Healthcare, USA). After desalting, an excess of ferritin was mixed with a solution of pyridyl disulfide-I@P that had been diluted with the conjugation buffer (0.1 M PBS, pH 7.8). After a continuous 24 h mechanical stir in an ice bath and subsequent centrifugation, the ferritin was linked to the I@P surface (I@P-ss-FRT) via a disulfide bond through a disulfide exchange reaction.

2.5. Synthesis of PDA nanoparticle

PDA nanoparticles were synthesized according to the previously reported method with minor modifications [42]. In brief, 9 mL of deionized water was mixed with 0.4 mL of ammonia water, 4 mL of ethanol, and held at 30 °C with magnetic stirring for 0.5 h. Afterward, 40 mg dopamine hydrochloride dissolving in 1 mL deionized water was speedily injected into the above-mentioned solution, and the reaction was allowed to run its course overnight. The resultant solution was precipitated using three times the volume of acetone and centrifuged (800 g, 8 min) to obtain PDA nanoparticles (about 50 nm particle size).

2.6. Characterization of as-synthesized I@P and I@P-ss-FRT

The particle size distribution and zeta-potential were analyzed by the dynamic light scattering (DLS) performed on the Zetasizer Nano ZS device. Transmission electron microscopy (TEM) was operated on JEM-2100F (JEOL Ltd, Japan) equipped with the energy dispersive spectroscopy (EDS) analyzer (Oxford INCA energy) to observe the morphologies and elemental composition of different nanoparticles. Fourier-transform infrared spectroscopy (FTIR, Nicolet™ iS5, Thermo Fisher Scientific Inc, MA, USA) was employed to determine the functional groups of nanoparticles, and the ultraviolet–visible (UV–vis) spectra were recorded on a UV–vis spectrophotometer (Shimadzu, Tokyo, Japan).

Western blot analysis was carried out to check that the ferritin was attached to the surface. Untreated commercial ferritin, I@P, and I@P-ss-FRT were lysed using cell lysis buffer and then heated to 95 °C for 5 min in SDS loading buffer. After that, 20 μL samples underwent electrophoresis using 15 % SDS-PAGE gel at 120 V until the bromophenol blue nearly reached the bottom of the gel. Afterward, the gel was transferred to a nitrocellulose membrane (Millipore, USA) at 250 mA for 1 h. After blocking by 5 % non-fat milk for 1 h, the blot was incubated with a primary antibody of ferritin light chain (1:10000) at 4 °C overnight and a secondary antibody for 1 h at room temperature, followed by determination using enhanced chemiluminescence assay. At last, the blot was developed using the FluorChem M imaging system.

The MR imaging capability of I@P and I@P-ss-FRT were analyzed using a 11.7T Bruker BioSpin MRI animal instrument (Institute of Science and Technology for Brain-Inspired Intelligence, Fudan University, Shanghai, China). T2-weighted images of I@P and I@P-ss-FRT at different Fe concentrations were recorded for T2 relaxation rate (r2) assessment.

The Fe^{2+} concentration of different nanoparticles was measured by a colorimetric assay based on 1,10-phenanthroline-ferrous ion complexes as a well-established method [43].

To assess the photothermal performance of different nanoparticles, 200 μL nanoparticle water solution was placed in a 0.5 mL tube under continuous exposure of an 808 nm laser (1.25 W/cm^2, Changchun New Industries Optoelectronics Technology Co., China) for 7 min. During this procedure, the change of temperature was monitored by a digital thermometer (TM-902C, Lutron Electronic Enterprise Co., Ltd, China) and photographed with an infrared thermographic camera (CEM Thermal Imager DT-980, Shenzhen Everbest Machinery Industry Co., Ltd, China).

2.7. In vitro Fe^{2+} release profile

In vitro Fe^{2+} release profile was quantified by 1,10-phenanthroline assay. In detail, different nanoparticle solutions were injected into the medium under various conditions to a final concentration of 50 μg Fe/mL and the photothermally treated groups were illuminated by an optical fiber-coupled 808 nm (laser power: 1.25 W/cm^2) for 5 min. The experiment was conducted on a shaker at a speed of 120 revolutions per minute (rpm) at a temperature of 37 °C. At preset time points, the sample was centrifuged at 20000 rpm for 5 min. 100 μL of the supernatant was collected for quantitative detection, and the same volume of

the fresh medium under different conditions was supplemented. The withdrawn supernatant was mixed with 500 μL of ammonium acetate buffer (0.1 M, pH 5.0) containing 1 % 1,10-phenanthroline (by weight). After a 15-min reaction, the absorbance reading at 510 nm was measured on a microplate reader (Synergy H1 Hybrid Multi-Mode Reader, BioTek Instruments, USA) and the iron concentration was calculated from a standard curve.

2.8. Extracellular GSH consumption

I@P or I@P-ss-FRT aqueous solutions were re-dispersed in 10 mM GSH solution and either exposed or not exposed to1.25 W/cm^2, 5 min of 808 nm laser irradiation. After being incubated for 12 h, the supernatant was spun-collected for 5 min at a speed of 20,000 rpm and then reacted with 5,5′-dithiobis-(2-nitrobenzoic acid) (DTNB). Then the absorbance of the solution at 405 nm was read using a microplate reader.

2.9. Cellular uptake and tumor spheroid penetration study

After being grown on confocal dishes overnight, MCF-7 and MCF-7/ADR cells were treated with I@P-FITC and I@P-ss-FRT-FITC in FBS-free RPMI-1640 for 4 h. Following a gentle three-time washing with pre-cooling PBS, the cells were observed under confocal laser scanning microscopy (CLSM, Carl Zeiss LSM710, Zeiss, Germany).

A previously-validated liquid overlay method was used to create MCF-7/ADR tumor spheroids [44]. Briefly stated, single-cell suspension (4×10^4 cells/mL) was seeded in 2 % agarose-coated 96-well plates with FBS-free RPMI-1640 supplemented with 5 μg/mL insulin, 20 ng/mL rh-EGF, 20 ng/mL rh-bFGF, 1 × B-27, and the cultivation process continued until the tumor spheroids with diameters of approximately 400 μm were formed. Then the tumor spheroids were co-cultured with I@P-FITC and I@P-ss-FRT-FITC for a further 4 h while being protected from light. At last, the tumor spheroids were washed with prechilled PBS and transferred to glass-bottom confocal dishes for Z-stack confocal imaging.

2.10. Assessment of in vitro cytotoxicity and synergic therapeutic efficacy

L929, MCF-7, and MCF-7/ADR cells were seeded in 96-well plates at a density of 8×10^3 cells/well. The initial culture media was aspirated from the wells after an overnight incubation period, and a fresh medium containing I@P or I@P-ss-FRT with different Fe concentrations was added. The wells were then co-incubated for an additional 24 h. Cell viabilities were estimated by CCK-8 according to the manufacturer's protocol.

MCF-7 and MCF-7/ADR cells were cultivated in 96-well plates for one night and subjected to the following treatments to test the efficiency of synergistic therapy: fresh media (as a control group), I@P, I@P/DFOM, I@P/Z-VAD-fmk, I@P-ss-FRT, I@P-ss-FRT/DFOM, and I@P-ss-FRT/Z-VAD-fmk (the concentrations of I@P and I@P-ss-FRT were 50 μg Fe/mL, DFOM was 50 μM, and Z-VAD-fmk was 50 μM), and cells in PTT groups were subjected to an 808 nm laser irradiation at 1.25 W/cm^2 for 5 min after 4 h of culture. The CCK-8 assay was run after 24 h to evaluate cell proliferation inhibition.

By distinguishing between live and dead cells, the Calcein AM/PI cell viability/cytotoxicity assay was applied to directly visualize the synergistic antitumor impact. MCF-7 and MCF-7/ADR cells were cultured in confocal dishes following the same incubation and PTT procedures as previously mentioned. Afterward, 1 mL testing buffer of Calcein AM/PI was added and stained for 30 min at 37 °C in the dark. Lastly, fluorescence images were captured using CLSM.

2.11. Determination of intracellular GSH level

The MCF-7/ADR cells were treated by I@P and I@P-ss-FRT with or without 808 nm laser illumination. After incubation overnight, the cells were harvested, and several cycles of freezing and thawing were used to prepare cell lysates. The GSH was then analyzed with GSH detection kit.

2.12. Determination of intracellular iron release

FerroOrange, an intracellular Fe^{2+} probe, was utilized to assess the ability of nanoparticles to release ferrous ions within cells. To be more precise, 24 μg of FerroOrange was dissolved in 35 μL of DMSO to create a 1 mM FerroOrange solution, and with further dilution a final concentration of 1 μM with the serum-free medium. MCF-7/ADR cells cultured in confocal dishes overnight were incubated with blank complete medium, I@P, and I@P-ss-FRT (50 μg Fe/mL). After a 4-h incubation with iron-based nanoparticles and subsequent washing with PBS, a NIR laser of 808 nm at a density of 1.25 W/cm^2 was induced to PTT groups for 5 min. About 4 h after the laser irradiation, the cells were rinsed with free RPMI-1640 three times and stained with 1 μM FerroOrange, followed by an additional 30 min of dark-incubation at 37 °C. Finally, the cells were observed and imaged under CLSM.

2.13. Determination of GPX-4 activity

MCF-7/ADR cells were seeded at a cell density of 1×10^5 cells/well in 12-well plates. 24 h after seeding, I@P and I@P-ss-FRT in RPMI-1640 (50 μg Fe/mL) were added, and after another 4 h, cells were irradiated by an 808 nm laser beam (1.25 W/cm^2, 5 min). Cells were harvested using cell scrapers after being grown for the night before being lysed with cell lysis buffer supplemented with PMSF and an enzyme inhibitor. Total protein concentration was then determined using a BCA kit. The western blot assay protocols used to measure the GPX-4 level were the same as those described in Section 2.6. with the following exceptions. Transfer membrane: 250 mA, 1 h. Primary antibodies: anti-GPX-4 antibody (1:1000), β-actin mouse monoclonal antibody (1:1000).

2.14. Cellular ROS and LPO measurement

The amount of generated ROS due to PTT treatment and the Fenton-like reaction of iron-based nanoparticles was determined by measuring the fluorescence of DCF oxidized from DCFH-DA by ROS. The MCF-7/ADR cells were plated in confocal dishes 24 h before the assay. After 4 h of preincubation with I@P, I@P/DFOM, I@P-ss-FRT, and I@P-ss-FRT/DFOM (the concentrations of iron-based nanoparticles were 50 μg Fe/mL, and DFOM was 50 μM), cells were loaded with DCFH-DA at working concentrations for 0.5 h in the dark after which cells were rinsed with free RPMI-1640 to remove unreacted fluorescent probes and the PTT groups exposed to an 808 nm laser (1.25 W/cm^2, 5 min). Then, CLSM was used to observe the fluorescence signals.

The FCM assay was also performed to quantify ROS levels. The day before the assay, MCF-7/ADR cells were inoculated in 12-well plates and cultured to 70–80 % confluence before being treated as mentioned above. Then, cells were separated into single-cell suspensions by trypsinization and detected by FCM under the FITC channel.

Blank complete RPMI-1640, I@P, I@P + laser, I@P/DFOM + laser, I@P-ss-FRT, I@P-ss-FRT + laser, and I@P-ss-FRT/DFOM + laser, each at a concentration of 50 μg Fe/mL for iron-based nanoparticles, 50 μM for DFOM, and a laser power of 1.25 W/cm^2 for 5 min, were applied to the MCF-7/ADR cells overnight. Then, cells were washed with PBS and fixed in a stationary liquid. Subsequently, a 10 μM BODIPY lipid probe was used to stain cells for 30 min away from light, followed by staining with Hoechst for 10 min. Finally, cells that had been loaded with LPO probes were either observed under CLSM or harvested for FCM detection.

2.15. Determination of mitochondrial membrane potential (ΔΨm)

The ΔΨm was determined using a JC-1 assay kit. After treated by I@P and I@P-ss-FRT with or without 808 nm laser illumination, MCF-7/ADR cells were stained with JC-1 for 30min followed by CLSM

observation and FCM detection.

2.16. Determination of intracellular malondialdehyde (MDA) level

The MCF-7/ADR cells were treated by I@P and I@P-ss-FRT with or without 808 nm laser illumination. After incubation overnight, the cells were lysed with cell lysis buffer supplemented with PMSF and an enzyme inhibitor. The MDA concentration was then analyzed using the MDA detection kit.

2.17. Animal models

Female Balb/c nude mice (weight: 16–18 g) were provided by the Laboratory Animal Center of Fudan University (Shanghai, China) and raised in specific pathogen-free conditions. Mice were acclimatized for a week. All animal assays were in accordance with the Guidelines for the Care and Use of Laboratory Animals of Fudan University. This study was approved by the Institutional Animal Care and Use Committee of the School of Pharmacy, Fudan University. To establish MCF-7/ADR xenograft models, 5×10^6/100 μL MCF-7/ADR cells were subcutaneously implanted into flanks of each mouse, and the tumor volumes monitored and calculated as $V = 0.5 \times (\text{tumor length}) \times (\text{tumor width})^2$. When tumor volumes were ~100 mm^3 ten days after inoculation, treatments were started.

2.18. In vivo tumor penetration study and MRI experiment

To investigate tumor tissue penetration, I@P-Cy5 and I@P-ss-FRT-Cy5 were peritumorally injected into mice, and the tumor sites subsequently irradiated with an 808 nm laser. 12 h after the different treatments, the tumors were dissected and frozen at optimal cutting temperatures (OCT) for cryosection. Then, slices were stained with DAPI and imaged under CLSM.

The *in vivo* MR experiment was performed on a 11.7T Bruker BioSpin MRI system. MR images were acquired before and after the injection of I@P or I@P-ss-FRT.

2.19. In vivo antitumor evaluation

The MCF-7/ADR tumor-bearing mice were randomized into 6 groups ($n = 5$), and peritumorally injected with PBS (G1, 80 μL), I@P (G2 and G4, 0.8 mg Fe/mL, 80 μL), I@P-ss-FRT (G3, G5, and G6, 0.8 mg Fe/mL, 80 μL). Shortly after I@P-ss-FRT injection, DFOM (120 mg/kg) was intraperitoneally administered to G6. Mice in G1, G4, G5, and G6 were illuminated by a fiber-coupled 808 nm with the laser spot adjusted to cover the whole tumor surface. Power density was kept at 1.25 W/cm^2 for 7 min, while the increase in tumor temperature was recorded by a thermography instrument. Body weights and tumor volumes were measured every two days. Mice were grown and monitored up until the tumor volume exceeded 1500 mm^3 on day 17. At the end of the experiment, mice were humanely euthanized after which the tumors and the main organs (heart, liver, kidney, lung, and spleen) were excised. The tumors were weighed while the excised organs were fixed, embedded, and sectioned for H&E staining.

2.20. Histochemical analysis

The same therapies outlined in Section 2.19. were applied to the nude mice carrying the MCF-7/ADR tumor. On the 2nd post-treatment day, mice were sacrificed via cervical dislocation and the tumors harvested. Partial tumors were prepared as tissue homogenates to measure GSH levels. The remaining tumors were fixed in 4 % paraformaldehyde and embedded in paraffin for GPX-4, BODIPY lipid probe, CD86, and CD206 immunofluorescence labeling. The last partial tumors were flash-frozen in liquid nitrogen and prepared as frozen sections for ROS assessment using Dihydroethidium (DHE) assay kit.

2.21. In vitro tumor-associated macrophage (TAM) polarization

The RAW 264.7 cells were cultured with 50 % 4T1 supernatants to generate M2 phenotype macrophages and with 20 ng/mL IFN-γ + 100 ng/mL LPS to induce M1 polarization. The RAW 264.7 cells that had not been treated were used as controls. The M2 macrophages were grown in experimental medium (DMEM containing I@P and I@P-ss-FRT, 50 μg Fe/mL), and after 4 h of co-incubation, cells in photothermally treated groups were irradiated by a continuous laser at 808 nm (1.25 W/cm^2, 5 min). Then, cells were incubated overnight, washed with PBS, detached using a cell scraper for FCM (stained with rat anti-mouse CD86 and CD206 monoclonal antibodies, respectively, according to manufacturer-recommended concentrations and procedures), and for western blotting (specific western blotting procedures were in line with those in Section 2.6. with the exception that the concentration of the separation gel was 8 %, the condition of membrane transfer was 100 V for 1.5 h, and the antibodies were MRC1 rabbit polyclonal antibody (1:1000) and β-actin mouse monoclonal antibody (1:1000)).

2.22. Statistical analysis

Data are presented as mean ± standard deviation (SD) for at least $n = 3$. Comparisons of means between and among groups were performed by the student's t-test and ANOVA respectively. *n. s.* is denoted as not significant ($P \geq 0.05$), while $P < 0.05$ (*), $P < 0.01$ (**), and $P < 0.001$ (***) were considered significant, very significant and highly significant, respectively.

3. Results and discussion

3.1. Fabrication and characterization

As shown in the flow chart of I@P-ss-FRT (Fig. S1), formation of the PDA coating was accomplished via Michael-Type addition, and conjugation of ferritin was the result of disulfide exchange reactions with pyridyl disulfide-I@P [38,45]. Various techniques were used to confirm successful preparation of I@P and I@P-ss-FRT. A typical TEM image for IONP (Fig. 2A) exhibited a spherical appearance in a monodisperse state with a size of 11.89 ± 2.73 nm (randomly selected 10 nanoparticles). Under alkaline condition, dopamine monomers which contained amine groups reacted with the carboxyl groups of DMSA-IONP to form a PDA coating shell. As revealed by TEM analysis (Fig. 2A), the obtained I@P exhibited a black IONP core and a gray PDA shell with a thickness of about 3 nm, as calculated by Image J. The DLS results (Fig. S2) revealed that hydrodynamic sizes of nanoparticles slightly increased from 14.10 ± 1.02 nm for IONP to 48.58 ± 4.821 nm for I@P. The comparatively bigger sizes revealed by DLS compared to those revealed by TEM analysis were attributed to hydration of the PDA layer. The zeta-potentials (Table S1) also changed with PDA coating, from −36.3 ± 0.282 mV to −22.2 ± 0.737 mV, which was due to deprotonation of catechol groups in the PDA shell. After further reactions with pyridyl disulfide cysteamine·HCl, the UV–vis absorbance spectra for the nanoparticles (Fig. S3) revealed characteristic pyridine group peaks at 232 nm and 282 nm, implying successful introduction of pyridyl disulfide groups. After ferritin decoration, DLS analysis (Fig. S2) revealed a considerable increase in particle sizes (~25 nm), which was roughly twice the diameter of ferritin, while the zeta-potential of I@P-ss-FRT was −19.6 ± 0.495 mV (Table S1). Due to the lower contrast compared to the I@P, ferritin conjugated in I@P-ss-FRT was rarely visible and only a slight increase in thickness of gray shells could be observed in the TEM image (Fig. 2A). However, after negative staining with uranyl acetate, they retained the typical hollow cage-like morphology with black nucleus and surrounded the periphery of the spheroid which distinguished them from the negatively-stained I@P (Fig. 2A) and the monodisperse state of commercially untreated ferritin [46]. Further evidence that ferritin had been conjugated to nanoparticles was provided by the appearance of

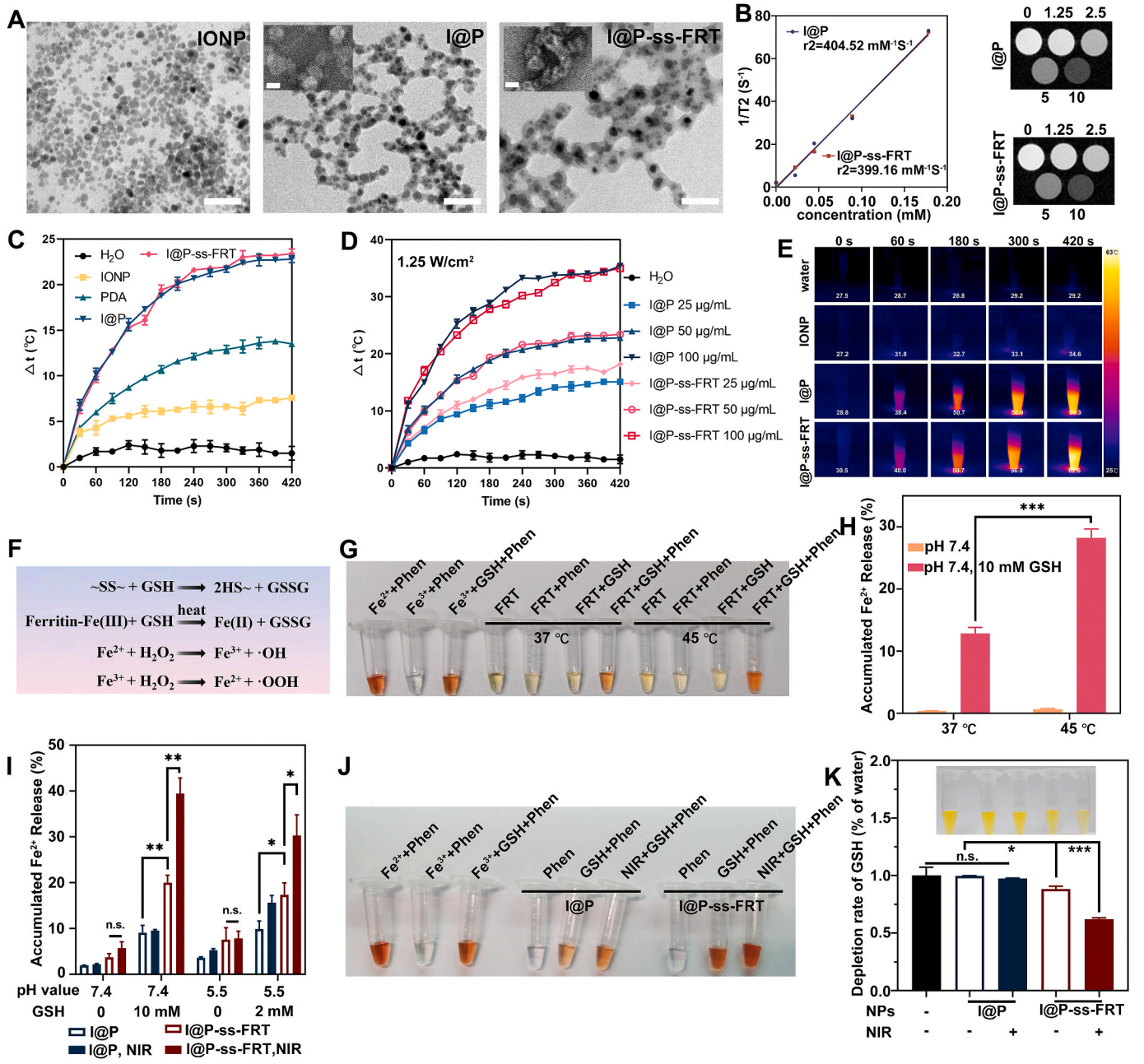

Fig. 2. Characterization of I@P-ss-FRT formulations. (A) TEM images of IONP, I@P, and I@P-ss-FRT; Scale bars: 50 nm. The insets show the negatively-stained samples; Scale bars: 20 nm. (B) T2 relaxation rates (r2) of I@P and I@P-ss-FRT at a series of Fe concentrations (left) and the T2-weighted maps for I@P (upper right) and I@P-ss-FRT (lower right). (C) Heating profile of IONP (50 μg Fe/mL), PDA (120 μg/mL in terms of nanoparticle concentration), I@P (50 μg Fe/mL, corresponding to 120 μg/mL in terms of nanoparticle concentration), and I@P-ss-FRT (50 μg Fe/mL) in water suspension under non-stop 808 nm irradiation for 420 s ($n = 3$). (D) The photothermal performance of I@P and I@P-ss-FRT at different Fe concentrations under the irradiation of an 808 nm laser with a power density of 1.25 W/cm^2 ($n = 3$). (E) Representative infrared thermal images of water, IONP, I@P, and I@P-ss-FRT (50 μg Fe/mL) with NIR illumination (808 nm, 1.25 W/cm^2, 420 s). (F) An illustration of reductive mobilization of ferrous ions from ferritin through GSH depletion and ROS level elevation. Colorimetric observation (G) and quantitative results (H) of Fe^{2+} released from ferritin under GSH and hyperthermal environments ($n = 3$). (I) Quantitative results of I@P and I@P-ss-FRT after 12 h incubation with different conditions ($n = 3$). (J) Colorimetric observation of Fe^{2+} released from nanoparticles in solutions with pH 7.4 following GSH addition and laser treatment. (K) GSH consumption in the solution after treatment with I@P and I@P-ss-FRT in the presence or absence of NIR irradiation, inset: optical photo of the DTNB color after different treatments ($n = 3$). (For interpretation of the references to color in this figure legend, the reader is referred to the Web version of this article.)

phosphorous and the increasing fraction of sulfur in EDS patterns (Fig. S4) [47,48]. Western blotting (Fig. S5) revealed that a clear band in I@P-ss-FRT after lysis, which was identical to that of the purified ferritin as the control group, while there were no obvious protein signals in I@P, suggesting the incorporation of ferritin. To further characterize PDA and ferritin in nanoparticles, FTIR was carried out to identify the chemical signatures and vibrational modes of IONP, I@P, and I@P-ss-FRT (Fig. S6). The band presented in all iron-based nanoparticles at 590 cm^{-1} was attributed to Fe–O vibration. Compared with IONP, the absorption related to aromatic rings (1626 cm^{-1} and 1507 cm^{-1} for benzene skeleton vibration, 803 cm^{-1} for C–H out-of-plane bending vibration) and the band assigned to primary amine (1263 cm^{-1} for

primary amine vibration, 1055 cm^{-1} for N–H in-plane bending vibration) proved the deposition of PDA shell. Meanwhile, two protein absorption peaks, at 1652 cm^{-1} and 1543 cm^{-1}, which was contributed to the C═O stretching vibration, N–H bending and C–N stretching vibration respectively, appeared in the spectra of I@P-ss-FRT, confirming that ferritin had been conjugated into the surface of I@P.

The as-synthesized I@P and I@P-ss-FRT retained stable and fine-dispersion conditions in both water and complete cell culture medium (10 % FBS-contained RPMI 1640) over 7 days at 4 °C under storage conditions. Moreover, at both pH 6.0 and pH 7.4 at 37 °C, I@P-ss-FRT maintained stable within 24 h, indicating the satisfactory durability of I@P-ss-FRT during cell culture and peritumoral injection (Fig. S7).

3.2. Multifunctional performance of I@P-ss-FRT

Prior to further cell and animal studies, various assays were performed to assess the MR imaging and photo-thermal energy conversion abilities of I@P and I@P-ss-FRT. Fig. 2B shows the obvious darkening effect of I@P and I@P-ss-FRT as the Fe concentration increased. Calculated through the curve fitting of 1/T2 as a function of Fe concentrations, I@P and I@P-ss-FRT had similar r2 value (404.52 $mM^{-1}S^{-1}$ and 399.16 $mM^{-1}S^{-1}$, respectively), suggesting the ferritin modification did not compromise the MR imaging functionality.

The different nanoparticles were continuously illuminated with an 808 nm laser (1.25 W/cm^2) for 420 s while the temperature in real time was recorded by a digital thermometer and a NIR thermal imager (Fig. 2C and E). In Fig. 2C, it is shown that irradiating I@P and I@P-ss-FRT increased their temperatures by ~22 °C, which was higher than those of IONP and PDA nanoparticles of the same size (~7 °C and ~14 °C, respectively), whereas the temperature of pure water, used as the negative control, showed minor elevations. Fig. S8 indicates that ferritin at different concentrations failed to raise their temperatures upon NIR irradiation. These findings imply that the photothermal effects could be amplified by the PDA shell but were not influenced by ferritin. Fig. 2D and S9 show that the photothermal conversion abilities of I@P and I@P-ss-FRT exhibited concentration and laser power dependence. According to the irradiation heating and cooling period and UV–vis absorption at 808 nm (Figs. S10 and S11), the photothermal conversion efficiency (**Text S1**) of I@P and I@P-ss-FRT were calculated to be 13.13 % and 13.24 %, respectively, similar as previously reported [39,49]. These results suggest I@P-ss-FRT could be effectively applied as MRI probe and photothermal agent.

As an endogenous antioxidant, GSH has the potential to directly scavenge for reactive oxygen species and act as a cofactor of various enzymes, including GPX-4, which is crucial in repairing lipids by breaking down LPO into harmless forms [50–52]. Therefore, relatively high GSH levels in tumor cells (up to 10 mM) inhibit ferroptotic cell death. Based on primary findings on iron release properties of ferritin, I@P-ss-FRT suppressed GSH levels via two pathways (Fig. 2F). First, disulfide ligands suppressed GSH levels via thiol-disulfide exchange reaction [53,54]. As shown in Fig. S12, under centrifugation, I@P in the GSH solution and I@P-ss-FRT in water were precipitated as a black and compact pellet at the bottom of the centrifuge tube, whereas I@P-ss-FRT in the GSH solution exhibited a different morphology, with a brown and uneven precipitation adhering to the tube wall, indicating the GSH-responsive feature of I@P-ss-FRT and the presence of disulfide bonds.

Second, under heat activation, reductant-dependent release of Fe^{2+} from ferritin contributes to substantial Fe^{2+} generation and GSH depletion. First, we verified whether Fe^{2+} release characteristics of ferritin might be influenced by the redox and hyperthermia environment by phenanthroline (Phen) assay, which is a Fe^{2+} chelator with the ability to form an orange-colored complex. In Fig. 2G, upon Phen addition, ferritin under 37 °C and 45 °C preserved its mild yellow hue after Phen addition, proving that there were no identifiable ferrous ions in solutions. The solution colored orange and 12.86 % Fe^{2+} was liberated when GSH was added to reduce the ferritin mineral towards soluble Fe^{2+} (Fig. 2H). The color became darker and a 2.19-fold enhancement (12.86 %–28.22 %) in Fe^{2+} release was observed in the GSH solution at 45 °C, compared to that at 37 °C. As illustrated in Fig. S13, rapid Fe^{2+} release occurred once at hyperthermic temperature. When the temperature is lowered, the rapid Fe^{2+} release was continued for another 20 min and became slow. These results confirm the significance of hyperthermia on promotion of iron release from ferritin in presence of GSH.

Then, we monitored the ferrous iron release profile of I@P and I@P-ss-FRT at different conditions (pH 7.4, 10 mM GSH to simulate the reductive state of tumor cells; pH 5.5, 2 mM GSH to mimic the reductive condition in lysosomes) with or without NIR illumination [55]. The results (Fig. 2I and J, and S14) show that the release rate of I@P was pH- and GSH-dependent, and the laser irradiation slightly elevated iron release, which may be attributed to acidic degradation of IONPs, thermal stability and acid sensitivity of the PDA layer [56–58]. Under identical conditions, nearly two-fold as many extra ferrous ions were detected in the I@P-ss-FRT solution as in the I@P, revealing the effects of ferritin conjugation. The most intriguing outcome is that when exposed to laser irradiation, the Fe^{2+} release rate of I@P-ss-FRT was greatly enhanced, increasing from (20.03 ± 1.58) % to (39.46 ± 3.35) % at pH 7.4 with 10 mM GSH and from (17.32 ± 2.66) % to (30.31 ± 4.48) % at pH 5.5 with 2 mM GSH. This may be because hyperthermia enhanced the opening of channels on the ferritin shell and thereafter facilitated the entry of reducing agent (GSH) into the ferritin core to release iron according to literature [26,27,31–33,35]. The I@P-ss-FRT exhibited a biphasic Fe^{2+} release behavior in which the fast release in the first 4 h was most likely attributed to contribution of ferritin as its transient burst release under 10 min thermal incubation. The continuous sustained release afterward was mainly due to the slow release of ionic iron from IONPs core in acidic environments. Ferrous iron release dual-platforms with differing and complementary properties ensured the powerful and persistent effects in ferroptosis.

The GSH consumption rate was measured by the DTNB assay. In Fig. 2K, a slight but significant drop (11.64 % ± 2.27 %) in GSH levels was noted after adding I@P-ss-FRT, whereas GSH levels negligibly changed after the addition of I@P, regardless of whether NIR illumination was present or not (0.38 % ± 0.32 % and 2.58 % ± 0.43 %, respectively). Upon laser treatment, the GSH depletion rate in I@P-ss-FRT was significantly accelerated by NIR-mediated hyperthermia effects (38.02 % ± 1.24 % drop), consistent with results of iron release profiles. The combination of photothermal effects and ferritin for activating ferroptosis via the release of ferrous ions and GSH depletion were revealed by these findings.

3.3. In vitro cellular uptake and cytotoxicity study

Taking advantage of the reaction between FITC and uncyclized amine groups on PDA and ferritin, I@P and I@P-ss-FRT were equivalently modified with FITC to construct I@P-FITC and I@P-ss-FRT-FITC for cellular uptake assessment [59]. In Fig. 3A, the green fluorescence signals of I@P-ss-FRT from internalized FITC were noticeably brighter than those of I@P, regardless of cell lines, in tandem with earlier findings that breast cancers have high expression levels of SCARA5 with intrinsic binding to light-chain ferritin [37,60]. We also noted that the uptake of I@P-ss-FRT was about 2.65 times greater in MCF-7/ADR cells than in MCF-7 cells. To elucidate the possible mechanism for the differential cellular uptake of I@P-ss-FRT, the expression of SCARA5 in MCF-7 and MCF-7/ADR cells were further characterized by western blot assay. Fig. S15 shows that the SCARA5 were largely upregulated in MCF-7/ADR cells than that of MCF-7 cells. Thus, it is rational to speculate that the I@P-ss-FRT were preferentially internalized by MCF-7/ADR cells via ferritin-SCARA5 mediation.

Compared to the two-dimensional (2D) cell culture system, the three-dimensional (3D) model of tumor spheroids better reflects tumor pathophysiological conditions. Thus, the MCF-7/ADR tumor spheroids were

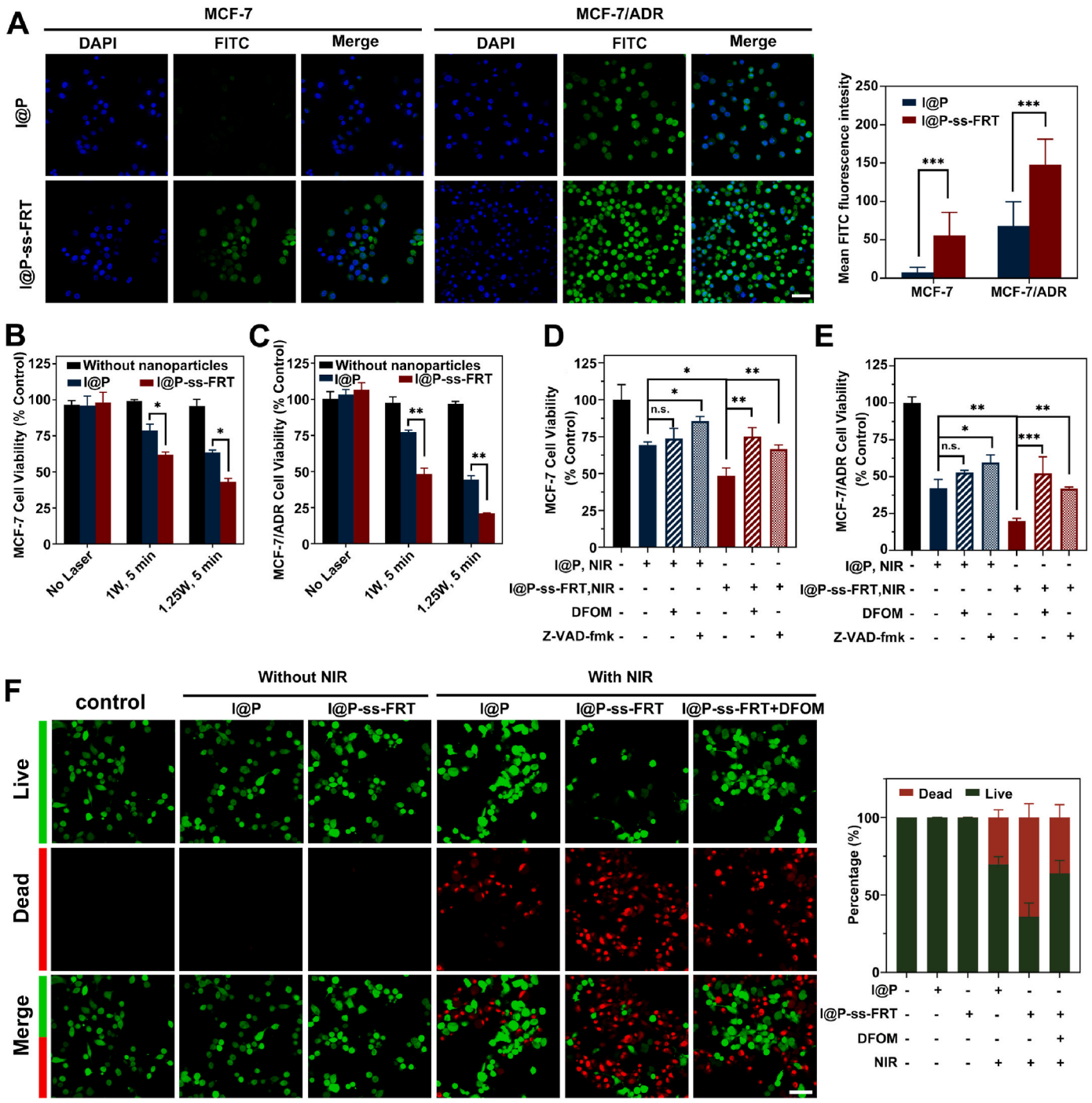

Fig. 3. The *in vitro* cellular evaluation of I@P-ss-FRT formulations. (A) CLSM images of MCF-7 and MCF-7/ADR cells after incubation with I@P-FITC and I@P-ss-FRT-FITC and the corresponding quantification of fluorescence FITC intensity inside cells; Scale bar = 50 μm ($n = 3$). (B) The viability of MCF-7 and (C) MCF-7/ADR cells after treatment with I@P and I@P-ss-FRT at 50 μg/mL Fe concentration or without nanoparticles under different NIR laser power densities ($n = 5$). (D) The viability of MCF-7 and (E) MCF-7/ADR cells after incubation with I@P, I@P-ss-FRT, I@P + DFOM, I@P + Z-VAD-fmk, I@P-ss-FRT + DFOM, and I@P-ss-FRT + Z-VAD-fmk (the concentrations of I@P and I@P-ss-FRT were 50 μg Fe/mL, DFOM was 50 μM, and Z-VAD-fmk was 50 μM) with NIR irradiation (808 nm, 1.25 W/cm^2, 5 min) ($n = 5$). (F) CLSM images of MCF-7/ADR cells stained with Calcein-AM and PI after different treatments. The ratio of Calcein-AM: PI fluorescence (live: dead cells) for 4 different views was determined using Image J; Scale bar = 50 μm.

built to assess the penetrative abilities of I@P and I@P-ss-FRT. Brighter fluorescent intensities were noted in the maximum-intensity projected image of tumor spheroid treated with I@P-ss-FRT than those of I@P (Fig. S16). The I@P penetrated tumor spheroids to a depth of 60.26 μm (~8 cell layers), while I@P-ss-FRT exhibited an average penetration depth of 88.08 μm (~10 cell layers). In summary, the enhanced drug-resistant cellular uptake and penetrative abilities of I@P-ss-FRT exhibited marked inhibitory effects on drug-resistant tumors.

Prior to *in vitro* antitumor efficacy evaluation, intrinsic cytotoxicities of I@P and I@P-ss-FRT to L929 cells, MCF-7/ADR cells, and MCF-7 cells were determined (Fig. S17). These results reveal that when the concentration of nanoparticles varied from 25 to 100 μg Fe/mL, neither I@P nor I@P-ss-FRT exhibited discernible cytotoxic effects to normal or tumor cells, and tumor cell viabilities were over 85 %. Based on

temperature elevation assay and other studies, a concentration of 50 μg Fe/mL was selected for follow-up assays [61].

To assess the photothermal cytotoxicities of I@P and I@P-ss-FRT to non-resistant tumor cells (MCF-7 as a model cell line) and drug-resistant tumor cells (MCF-7/ADR cells as a model cell line), two tumor cell types were incubated with I@P or I@P-ss-FRT for 4 h and exposed to different 808 nm laser irradiation regimens. In Fig. 3B and C, both I@P and I@P-ss-FRT exhibited laser-power-intensity-dependent photothermal cytotoxicities to MCF-7 cells and MCF-7/ADR cells, mapping against the power-intensity-dependent photothermal ability. Additionally, two interesting outcomes were revealed. First, compared to I@P, I@P-ss-FRT showed robust cell-killing effects on MCF-7 and MCF-7/ADR cells. Since the comparable photothermal performance of I@P and I@P-ss-FRT, it could be considered that I@P-ss-FRT + NIR and I@P + NIR maintained identical thermal cell-killing efficacies and that improvements in cytotoxicity were attributed to the I@P-ss-FRT-mediated ferroptosis induced by photothermal effects. Second, compared to non-resistant tumor cells, these therapeutic approaches were more cytotoxic to drug-resistant tumor cells. For instance, after 5 min of laser irradiation at 1.25 W/cm^2, only 63.42 % and 43.05 % of MCF-7 cells survived, while cell

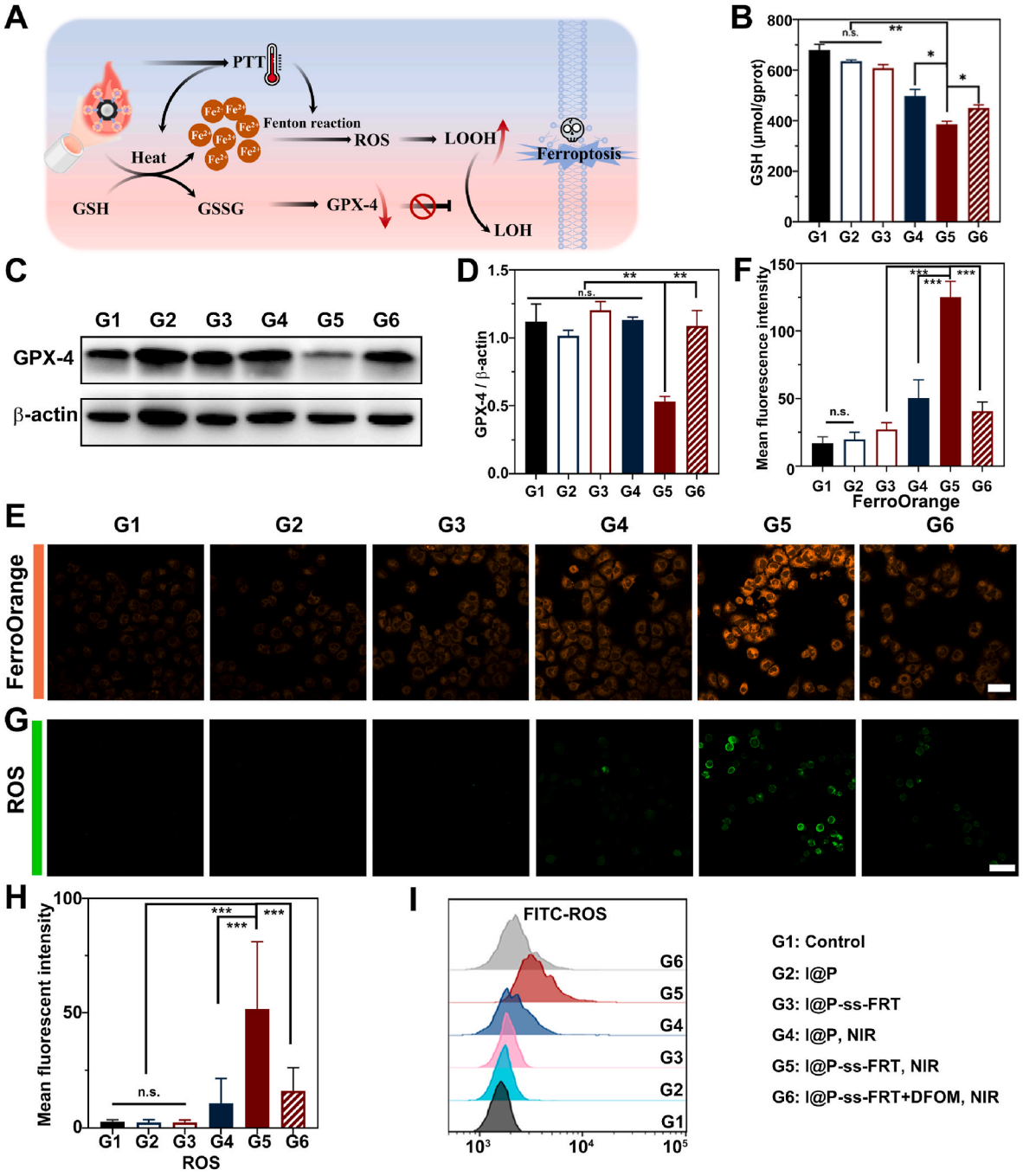

Fig. 4. The mechanisms underlying occurrence of ferroptosis. (A) A schematic illustration of GSH-triggered and PTT-enhanced ferroptosis. (B) GSH contents normalized to the total protein concentration in MCF-7/ADR cells after different treatments (n = 5). (C) Cellular protein expression of GPX-4 in MCF-7/ADR cells after treatments with I@P and I@P-ss-FRT (50 μg Fe/mL) with or without 808 nm laser exposure (1.25 W/cm^2, 5 min) and (D) the relative level of GPX-4/β-actin (n = 3). (E) CLSM images of MCF-7/ADR cells after incubation with I@P and I@P-ss-FRT showing intracellular Fe^{2+} ions levels using fluorescent probe FerroOrange and (F) the quantification of fluorescence intensity inside cells; Scale bar = 50 μm (n = 3). (G) CLSM images, (H) mean fluorescent intensity of the cells determined from the CLSM images, and (I) FCM analysis of ROS production in MCF-7/ADR cells after different treatments; Scale bar = 50 μm (n = 3).

viabilities of MCF-7/ADR dropped to about 44.31 % and 21.07 % when treated with I@P and I@P-ss-FRT, respectively. These differences were possibly attributed to the relatively high uptake of nanoparticles and stronger sensitivity of drug-resistant tumor cells to ferroptosis. Thus, the MCF-7/ADR cells were more susceptible to PTT of I@P-ss-FRT and its subsequent other tumor-fighting mechanisms.

Then, the ferroptosis inhibitor (DFOM as an iron-chelating compound) and apoptosis inhibitor (Z-VAD-fmk) were used to rescue cell death. Comparable findings were noted in both cell lines (Fig. 3D and E). Both DFOM and Z-VAD-fmk could block cell death in I@P-ss-FRT + NIR group, revealing the involvement of ferroptosis and apoptosis in antitumor effects of I@P-ss-FRT + NIR and the ferroptotic cell death was more pronounced than the apoptotic pathway. The absence of significant changes in cell viabilities between the I@P + NIR and I@P + NIR + DFOM groups suggested that the minimal GSH depletion and iron release by I@P alone were inadequate to result in ferroptotic cell death. In the meantime, cell ablation effects of I@P and I@P-ss-FRT were further determined by Calcein-AM/PI staining to visually reflect the percentage of live/dead cells (Fig. 3F and S18). The number of red-colored (dead) cells was higher in MCF-7/ADR cells than in MCF-7 cells that had received the same treatments. The red fluorescence was maximum in MCF-7/ADR cells treated with I@P-ss-FRT + NIR, which was alleviated after DFOM addition. In conclusion, I@P-ss-FRT' PTT activated ferroptosis, which promoted cell death. Thus, I@P-ss-FRT is a promising multifunctional photothermal agent for drug-resistant tumor therapy.

3.4. *In vitro mechanism of ferroptosis*

After establishing that the photothermal effects of I@P-ss-FRT induced ferroptosis, we assessed the mechanisms of ferroptosis. The proposed mechanisms underlying I@P-ss-FRT-induced PTT and ferroptosis are shown in Fig. 4A. The nanoparticle-mediated PTT acts together with GSH to trigger the release of ferrous ions and accelerates the kinetics of Fenton reaction. Meanwhile, GSH depletion coincides with GPX-4 inactivation, which makes LPO impossible to transform into non-poisonous forms, thereby inducing membrane rupture and ferroptosis. First, we investigated the ability of I@P-ss-FRT in intracellular GSH depletion. Fig. 4B shows that GSH levels in MCF-7/ADR cells incubated with I@P or I@P-ss-FRT slightly decreased but not significantly when compared with the control group, and decreased by ~26 % in the I@P group with 808 nm laser irradiation, in line with an earlier report that PDA exerted mild effects on GSH consumption [62]. I@P-ss-FRT with laser irradiation resulted in the most significant drop in cellular GSH levels (down to 56.76 %). Then, protein expressions of GPX-4, which is critical in the lipid repair process, was determined by the western blotting assay. In Fig. 4C and D, it is shown that despite their effects on GSH, treatment with I@P with or without NIR exposure, and co-incubation with I@P-ss-FRT did not markedly alter GPX-4 expressions. These results reveal that the presence of a lag between influences on GSH and changes in GPX-4 in tandem with findings from a previous study [63]. In contrast, I@P-ss-FRT plus NIR illumination significantly suppressed GPX-4 expressions in MCF-7/ADR cells, with expressions of 0.53 ± 0.01 (relative to β-actin). In Fig. S19, the loss of GPX-4 function induced by I@P-ss-FRT + NIR was more pronounced in MCF-7/ADR cells than that in MCF-7 cells, resulted in selective cell ferroptosis owing to the toxic effects of lipid peroxidation. These results indicate that the reduction of ferritin was concomitant with GSH depletion, which led to inactivation of GPX-4 and destruction of antioxidative defense mechanisms in drug-resistant cancer cells.

Then, we performed intracellular Fe^{2+} detection in MCF-7/ADR cells after different treatments using the FerroOrange fluorescent probe, which irreversibly reacted with Fe^{2+} to form orange fluorescent products. In Fig. 4E and F, after 4 h of co-incubation with I@P and I@P-ss-FRT, the MCF-7/ADR cells exhibited faint orange fluorescence when compared to the untreated group. Interestingly, the fluorescence intensity became brighter after NIR laser exposure and the cells in the I@P-ss-FRT + NIR group emitted the brightest fluorescence, implying that enlargement effects of the NIR laser on cellular Fe^{2+} release were more pronounced in I@P-ss-FRT. These results support the finding from *in vitro* Fe^{2+} release and further verify the release-promoting effects of TME and PTT.

Since the Fe^{2+} released from iron-based nanoparticles would react with the relatively high levels of H_2O_2 in tumor cells to produce ROS, the MCF-7/ADR cells with different treatments were dyed with an intracellular ROS probe (DCFH-DA) and processed by CLSM and FCM. In Fig. 4G-I, there were no visible green fluorescence in I@P-only and I@P-ss-FRT-only groups, due to the small number of Fe^{2+} after these two treatments. The ROS formation exhibited a minor increase after the laser was introduced to the I@P-incubated cells, which may be explained by the acceleration effect of high temperature due to PTT on the Fenton reaction speed [64–66]. The strongest green fluorescence in CLSM image and an obvious right shift in FCM result were seen in I@P-ss-FRT-incubated cells with laser exposure, which was attributed to co-actions of numerous Fe^{2+} released from ferritin in I@P-ss-FRT and PTT's acceleration on Fenton reaction. These outcomes were markedly suppressed when DFOM was added. Based on findings from semi-quantitative assessment, the mean fluorescence intensities of ROS in I@P-ss-FRT + NIR-treated cells were 18.98 times greater than those in the dark and 4.80 times greater than those in I@P + NIR-treated cells. Excessive ROS production can cause the dysfunction of mitochondria, manifested in ΔΨm reduction, which is a common warning of ferroptosis. As displayed in Fig. 5A and B, I@P and I@P-ss-FRT had negligible influence on the ΔΨm. The mitochondria were depolarized with I@P-ss-FRT + NIR as indicated by the noticeable increase of the JC-1 monomers. Flow cytometric measurement in the ratio of the green to red fluorescence also confirmed that the I@P-ss-FRT + NIR group significantly caused ΔΨm reduction (Fig. 5C).

After suppression of GPX-4 activity and elevation of ROS, we assayed the LPO levels, the most important marker of ferroptosis, using the C11 $BODIPY^{581/591}$ dye, whose maximum emission shifted from 590 nm (red) to 510 nm (green) upon LPO oxidization [67]. In Fig. 5D and E and S20, the CLSM and FCM results of LPO agree with ROS trends. The I@P-ss-FRT-treated cells irradiated with laser resulted in highest LPO generation with a 3.19-fold stronger green fluorescent signal than that of cells in control group and 2.09-fold to the I@P + NIR group. Specifically, when cells were treated with DFOM, the green fluorescence dimmed while the red fluorescent signal began to brighten. These phenomena confirm the hypothesis that ferroptosis is involved in I@P-ss-FRT + NIR-induced cytotoxicity, and was increased by PTT. Finally, as the final product of LPO, MDA levels were detected by MDA kit to verify the ability of I@P-ss-FRT + NIR to induce ferroptosis. As shown in Fig. 5F, the trend of the MDA content was similar to that of LPO. I@P-ss-FRT + NIR exposure remarkably increased the level of MDA in MCF-7/ADR cells. In summary, the cytotoxic effects of I@P-ss-FRT under NIR exposure were associated with ferroptosis via inhibition of GSH/GPX-4 and buildup of Fe^{2+}.

3.5. *In vivo antitumor study*

Given the findings from *in vitro* studies, I@P-ss-FRT was assessed *in vivo*. First, the penetrative abilities of the Cy5-labeled I@P and I@P-ss-FRT were investigated by cryosection of tumor tissues. In Fig. S21, only a limited amount of I@P with a weak fluorescent signal was concentrated in the tumor edge, while I@P-ss-FRT were able to deeply penetrate the periphery but also into the core areas of tumors. Meanwhile, PTT improved I@P and I@P-ss-FRT distributions, which were attributed to local damage of the extracellular matrix by PTT [68,69]. Thus, more I@P-ss-FRT infiltrated the tumor interior to potently exert antitumor effects. Moreover, the multifunctional I@P-ss-FRT could be applied as MRI probe utilizing the high transverse relaxivity of Fe_3O_4. Fig. S22 shows that significant T2 darkening effect, from the tumor

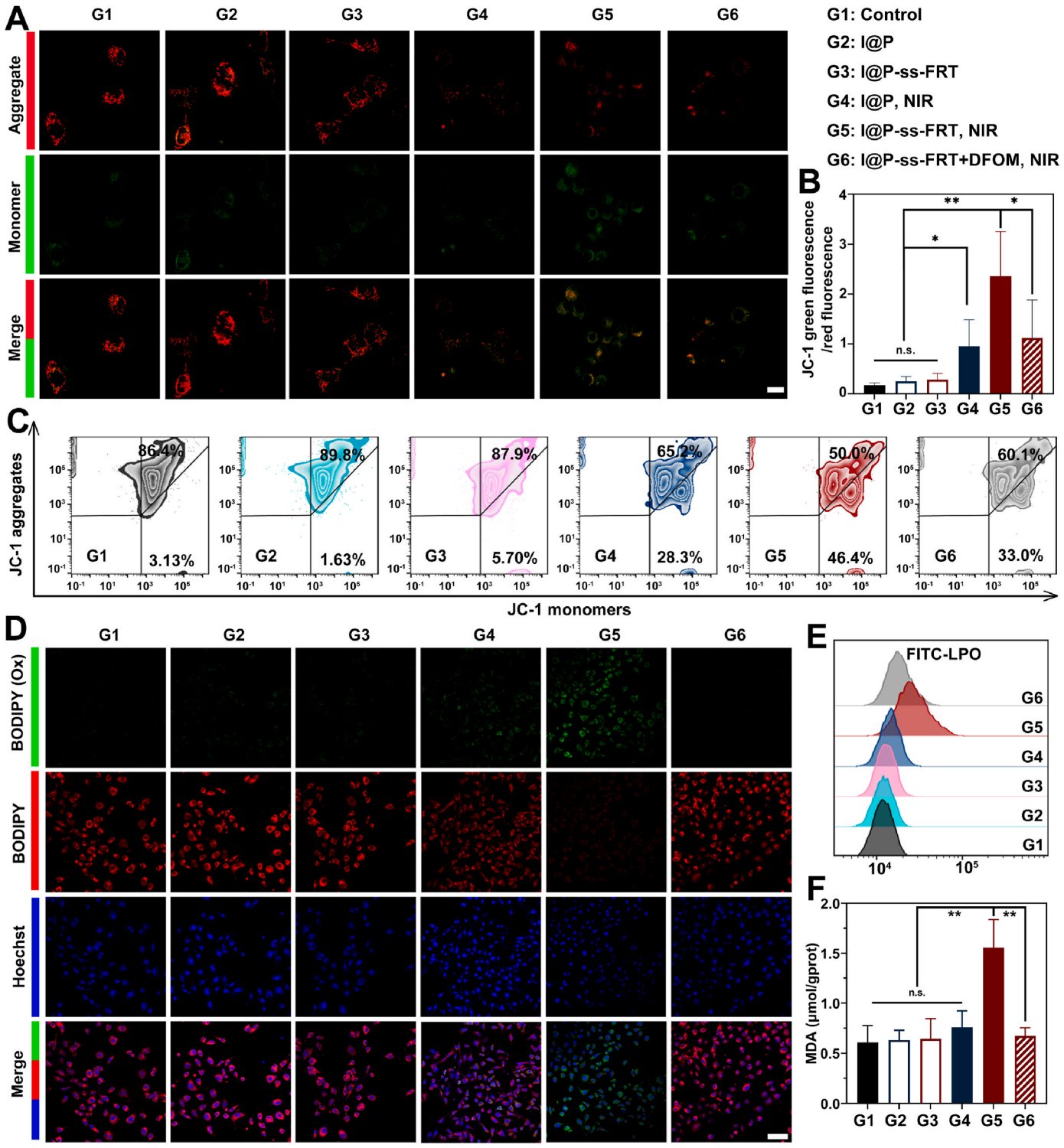

Fig. 5. The *in vitro* analysis of ferroptosis. (A) CLSM images of MCF-7/ADR cells after different treatments tested using JC-1 fluorescent probes, Scale bar = 20 μm. (B) Relative green/red fluorescence ratio of the cells determined from the CLSM images of JC-1 staining. (C) FCM analysis of JC-1 staining in MCF-7/ADR cells after different treatments ($n = 3$). (D) Determination of LPO generation in MCF-7/ADR cells after different treatments based on CLSM images; Scale bar = 50 μm ($n = 3$). (E) FCM results showing the LPO production in MCF-7/ADR cells after different treatments ($n = 3$). (F) MDA contents normalized to the total protein concentration in MCF-7/ADR cells after different treatments ($n = 5$). (For interpretation of the references to color in this figure legend, the reader is referred to the Web version of this article.)

edges toward the center, were observed for both mice after iron-based nanoparticles injection, implying the imaging capabilities of I@P and I@P-ss-FRT.

To establish the *in vivo* combined antitumor efficacies, MCF-7/ADR tumor-bearing nude mice were randomized into 6 groups and treated as: PBS + NIR (as a control group, G1), I@P (G2), I@P-ss-FRT (G3), I@P + NIR (G4), I@P-ss-FRT + NIR (G5), and I@P-ss-FRT + DFOM + NIR (G6) (Fig. 6A). Given that after intravenous injection, the marked uptake of I@P-ss-FRT by macrophages is detrimental to circulation time (Fig. S23), we selected peritumoral injection as a route for I@P and I@P-

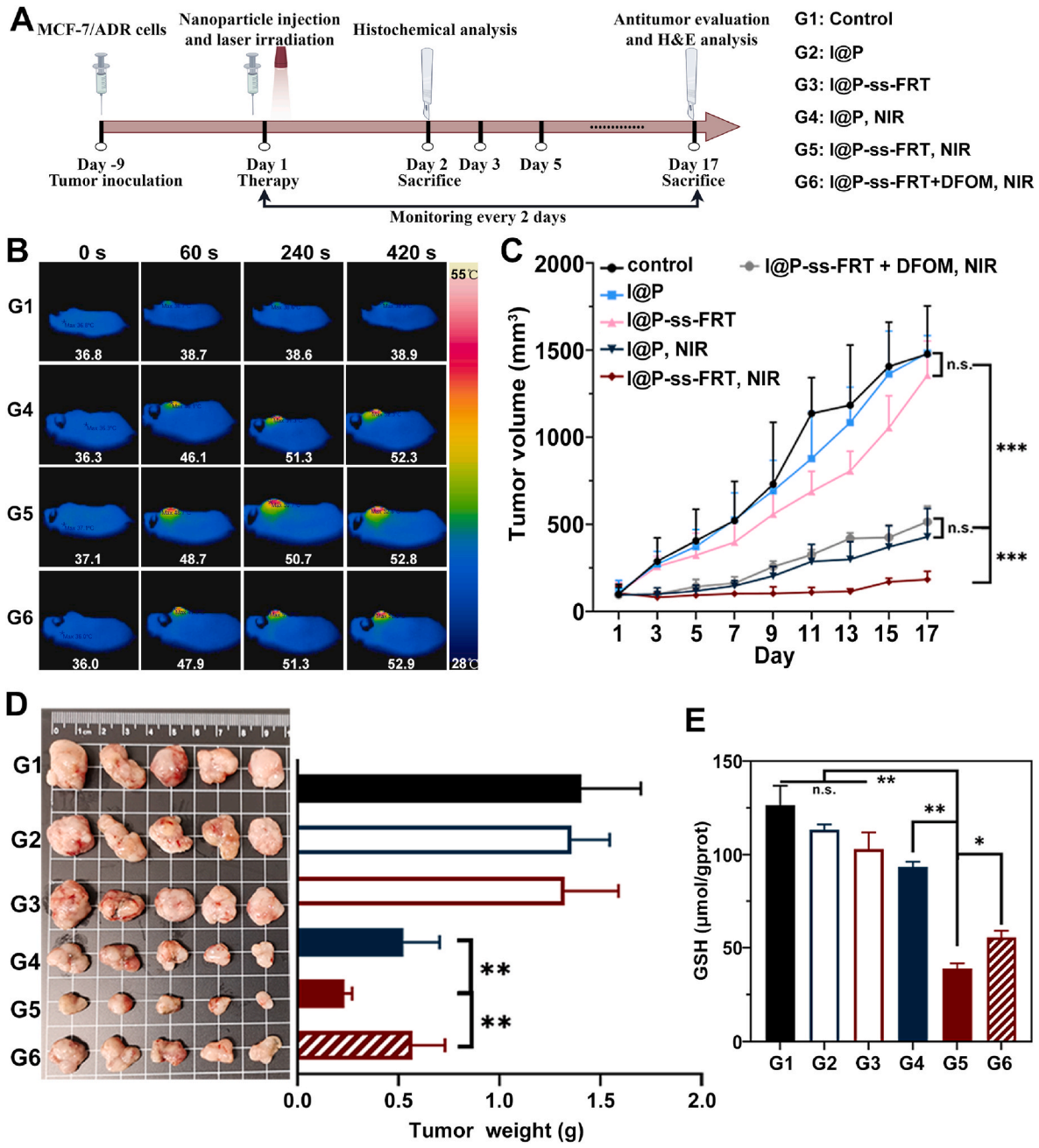

Fig. 6. The *in vivo* anti-tumor therapeutic effects of I@P-ss-FRT formulations. (A) Schematic illustration of the treatment schedules in MCF-7/ADR breast cancer model. (B) Representative infrared thermal images of MCF-7/ADR tumor-bearing mice exposed to 808 nm laser irradiation for 7 min after different treatments. (C) The tumor volume curves of MCF-7/ADR breast tumor-bearing mice after different treatments ($n = 5$). (D) Photo (left) and weight (right) of dissected tumors from mice from each group in the end of experimentation ($n = 5$). (E) GSH levels normalized to total protein concentration of MCF-7/ADR tumor tissues ($n = 5$).

ss-FRT (80 μL, 0.8 mg Fe/mL) administration, thereby bypassing systemic circulation and facilitating TAM polarization. At 4 h after injection, all G1, G4, G5, and G6 mice received identical 808 nm laser treatments, and the temperature rise in tumors were imaged by a thermal camera (Fig. 6B). The absence of temperature elevation in G1 indicated that low NIR absorption by tumor tissues did not produce enough heat. Meanwhile, due to similar photothermal performance and equivalent doses of I@P and I@P-ss-FRT, temperature increase profiles were comparable among the other groups, implying that the groups maintained identical thermal tumor-ablation efficacies and that improvements in overall antineoplastic effects were associated with underlying antitumor mechanisms. Fig. 6C shows the tumor growth tendencies every 2 d since the start of treatment. Both nanoparticle-treated alone groups (I@P and I@P-ss-FRT) failed to inhibit tumor growth and the tumor volume remained equivalent to that in the control group, whereas I@P + NIR exerted antitumor effects but was still inadequate to attain a decent suppression outcome. Among all groups, tumors in the I@P-ss-FRT + NIR significantly shrank, and these amplified antitumor effects could be blocked by the iron chelator (DFOM), which shows the contribution of ferroptosis. At the trial, tumors in each group of mice were excised, imaged, and weighed (Fig. 6D). The weights of tumors from G1-G6 were 1.40 g ± 0.29 g, 1.35 g ± 0.19 g, 1.32 g ± 0.26 g, 0.52 g ± 0.18 g, 0.23 g ± 0.03 g, and 0.57 g ± 0.16 g, respectively. Moreover, tumor-suppression abilities of I@P-ss-FRT + NIR were the most superior, with an inhibitory rate of 83.46 %. Tumor sizes in the I@P + NIR and I@P-ss-FRT + DFOM + NIR groups were comparable.

These results are in good conformity with the tumor growth curve. None of the groups exhibited obvious body weight losses (Fig. S24) and either was any serious damage observed in H&E slices of major organs (Fig. S25), which shows the *in vivo* safety of iron-based nanoparticles.

Finally, histochemical analyses supported the occurrence of NIR-mediated ferroptosis. In Fig. 6E, GSH levels in harvested tumors were moderately downregulated by 26.14 % in I@P + NIR group and markedly suppressed by 69.04 % in the I@P-ss-FRT + NIR group. Moreover, GPX-4 expressions were substantially reduced to 20.62 % when mice were treated with I@P-ss-FRT + NIR (Fig. 7A and B). After treatment of tumor-bearing mice with I@P-ss-FRT + NIR, ROS and LPO levels markedly increased by 57.30- and 339.47-fold, respectively, compared to the control groups. The elevations were neutralized by additional supplementation of DFOM (Fig. 7C-F). In contrast, compared to the control group, there were negligible changes in ROS and LPO levels in mice that had been treated with I@P or I@P-ss-FRT alone, while a slight increase was noted in the I@P + NIR group. Fe^{2+}, ROS, and PTT are functional in remodeling TAMs from the M2 phenotype to the M1 phenotype [19,70–72]. With regards to preferential uptake of I@P-ss-FRT by macrophages, we investigated whether treatment with I@P-ss-FRT + NIR affects TAM polarization. In Fig. 7G and H, it is shown that I@P-ss-FRT + NIR treatment activated macrophage polarization towards the M1 phenotype and markedly reduced the percentage of the green fluorescence area, which represents M2 type macrophages. We also verified the TAM polarization abilities of nanoparticles at the cellular level by western blotting (Fig. S26) and FCM (Fig. S27). The results were consistent with those obtained *in vivo*. In summary, the photothermal effects of I@P-ss-FRT provoke ferroptosis and alter TAM maturation, thereby suppressing the growth of drug-resistant tumors *in vitro* and *in vivo*.

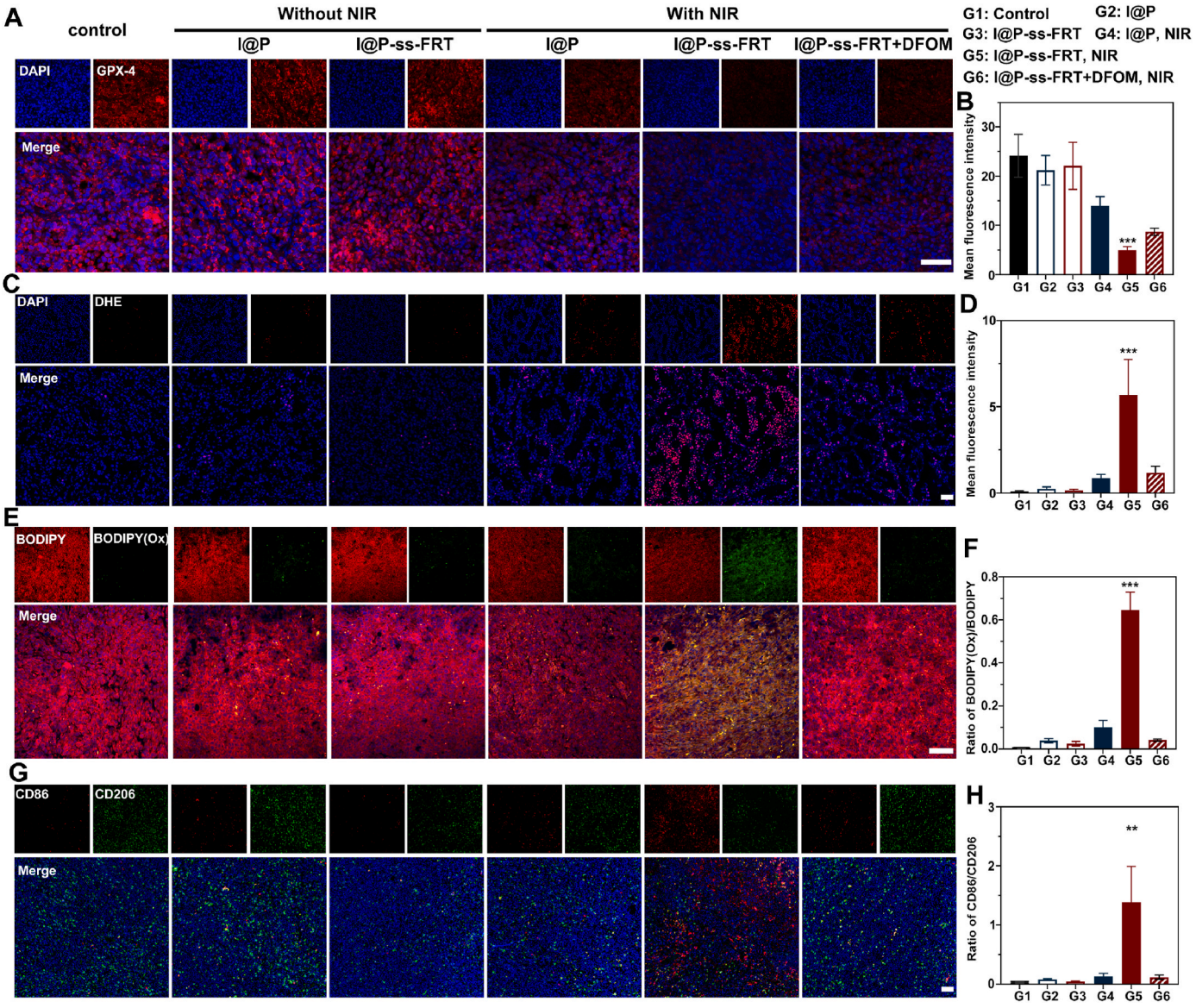

Fig. 7. Histochemical evaluation. (A) Immunofluorescence staining with antibodies against GPX-4 (red) and (B) the corresponding fluorescent intensity; Scale bar = 50 μm. (C) CLSM of ROS in tumor tissue stained with DAPI (blue color) and DHE (ROS fluorescent probe, red color) from each group and (D) CLSM-based mean fluorescent intensity of; Scale bar = 50 μm. (E) Immunofluorescence analysis with C11-BODIPY$^{581/591}$ probe (BODIPY(Ox), LPO, green; BODIPY, LP, red) and (F) the ratio of BODIPY(Ox)/BODIPY of 4 different views was calculated with Image J; Scale bar = 100 μm. (G) Representative images of tumor tissue stained by DAPI (blue color) and TAM (CD86, M1 maker, red color; CD206, M2 maker, green color) and (H) CLSM-based ratio of CD86/CD206; Scale bar = 100 μm. (For interpretation of the references to color in this figure legend, the reader is referred to the Web version of this article.)

4. Conclusion

In conclusion, we successfully represented a multifunctional nanoparticle (I@P-ss-FRT) to accomplish the combination of PTT and ferroptosis in drug-resistant breast cancer treatment. The I@P-ss-FRT had a diameter of approximately 70 nm with a PDA shell to improve the photothermal effect and a ferritin cloak as an iron storage material. The I@P-ss-FRT nanoparticle had localized photothermal cell-killing effect and excellent MR imaging ability. Taking advantage of the photothermal effect to accelerate Fe^{2+} release from ferritin in reductive TME accompanied by GSH depletion, significant photothermal-ferroptosis therapeutic outcome was observed in MCF-7/ADR cells than in MCF-7 cells, which was reversed by the ferroptosis inhibitor (DFOM), implicating the involvement of ferroptosis. *In vitro* assays showed that the I@P-ss-FRT nanoparticles improved cellular uptake, deep tumor spheroid penetration, substantive ROS and LPO generation, a notable downregulation of GPX-4 activity, and evident TAM polarization. As expected, Fe^{2+} accumulation and GSH consumption amplified the PTT-mediated ferroptosis and induced potent tumor-killing effects. Furthermore, I@P-ss-FRT plus NIR treatments exhibited marked anti-tumor outcomes in MCF-7/ADR xenograft-bearing mice. In this mutually beneficial treatment, PTT serves as a catalyst and an amplifier for ferroptosis, and ferroptosis, in turn, complements the anti-tumor effects of PTT, thereby achieving synergistic therapeutic effects in drug-resistant cancer. Therefore, this nanoparticle is promising for treatment of drug-resistant breast cancer.

CRediT authorship contribution statement

Yiting Chen: Writing – original draft, Methodology, Investigation, Formal analysis, Data curation, Conceptualization. **Xinhong Li:** Methodology, Data curation, Conceptualization. **Kuankuan Luo:** Methodology, Investigation. **Tao Wang:** Methodology, Investigation. **Tongyao Liu:** Methodology, Investigation. **Enhao Lu:** Validation, Investigation. **Rui Wang:** Formal analysis. **Yu Luo:** Formal analysis. **Xianyi Sha:** Writing – review & editing, Writing – original draft, Supervision, Funding acquisition, Conceptualization.

Declaration of competing interest

The authors declare that they have no known competing financial interests or personal relationships that could have appeared to influence the work reported in this paper.

Data availability

Data will be made available on request.

Acknowledgements

This work was supported by National Key R&D Program of the Ministry of Science and Technology of the People's Republic of China (2022YFC2304303) and the National Natural Science Foundation of China (81773201 and 81873893). We thank Home for Researchers (www.home-for-researchers.com) for the scheme drawing.

Appendix A. Supplementary data

Supplementary data to this article can be found online at https://doi.org/10.1016/j.mtbio.2024.101085.

References

[1] R.L. Siegel, A.N. Giaquinto, A. Jemal, Cancer statistics, CA A Cancer J. Clin. 74 (1) (2024) 12–49.
[2] N. Harbeck, F. Penault-Llorca, J. Cortes, M. Gnant, N. Houssami, P. Poortmans, K. Ruddy, J. Tsang, F. Cardoso, Breast cancer, Nat. Rev. Dis. Prim. 5 (1) (2019) 66.
[3] P. Vici, M. Brandi, F. Giotta, P. Foggi, F. Schittulli, L. Di Lauro, N. Gebbia, B. Massidda, G. Filippelli, D. Giannarelli, A. Di Benedetto, M. Mottolese, G. Colucci, M. Lopez, A multicenter phase III prospective randomized trial of high-dose epirubicin in combination with cyclophosphamide (EC) versus docetaxel followed by EC in node-positive breast cancer, GOIM (Gruppo Oncologico Italia Meridionale) 9902 study, Ann Oncol 23 (5) (2012) 1121–1129.
[4] R. Gray, R. Bradley, J. Braybrooke, Z. Liu, R. Peto, L. Davies, D. Dodwell, P. McGale, H. Pan, C. Taylor, W. Barlow, J. Bliss, P. Bruzzi, D. Cameron, G. Fountzilas, S. Loibl, J. Mackey, M. Martin, L. Del Mastro, V. Möbus, V. Nekljudova, S. De Placido, S. Swain, M. Untch, K.I. Pritchard, J. Bergh, L. Norton, C. Boddington, J. Burrett, M. Clarke, C. Davies, F. Duane, V. Evans, L. Gettins, J. Godwin, R. Hills, S. James, H. Liu, E. MacKinnon, G. Mannu, T. McHugh, P. Morris, S. Read, Y. Wang, Z. Wang, P. Fasching, N. Harbeck, P. Piedbois, M. Gnant, G. Steger, A. Di Leo, S. Dolci, P. Francis, D. Larsimont, J. M. Nogaret, C. Philippson, M. Piccart, S. Linn, P. Peer, V. Tjan-Heijnen, S. Vliek, J. Mackey, D. Slamon, J. Bartlett, V.H. Bramwell, B. Chen, S. Chia, K. Gelmon, P. Goss, M. Levine, W. Parulekar, J. Pater, E. Rakovitch, L. Shepherd, D. Tu, T. Whelan, D. Berry, G. Broadwater, C. Cirrincione, H. Muss, R. Weiss, Y. Shan, Y. F. Shao, X. Wang, B. Xu, D.-B. Zhao, H. Bartelink, N. Bijker, J. Bogaerts, F. Cardoso, T. Cufer, J.-P. Julien, P. Poortmans, E. Rutgers, C. van de Velde, E. Carrasco, M. A. Segui, J.U. Blohmer, S. Costa, B. Gerber, C. Jackisch, G. von Minckwitz, M. Giuliano, M. De Laurentiis, C. Bamia, G.-A. Koliou, D. Mavroudis, R. A'Hern, P. Ellis, L. Kilburn, J. Morden, J. Yarnold, M. Sadoon, A.H. Tulusan, S. Anderson, G. Bass, J. Costantino, J. Dignam, B. Fisher, C. Geyer, E.P. Mamounas, S. Paik, C. Redmond, D.L. Wickerham, M. Venturini, C. Bighin, S. Pastorino, P. Pronzato, M.R. Sertoli, T. Foukakis, K. Albain, R. Arriagada, E. Bergsten Nordström, F. Boccardo, E. Brain, L. Carey, A. Coates, R. Coleman, C. Correa, J. Cuzick, N. Davidson, M. Dowsett, M. Ewertz, J. Forbes, R. Gelber, A. Goldhirsch, P. Goodwin, D. Hayes, C. Hill, J. Ingle, R. Jagsi, W. Janni, H. Mukai, Y. Ohashi, L. Pierce, V. Raina, P. Ravdin, D. Rea, M. Regan, J. Robertson, J. Sparano, A. Tutt, G. Viale, N. Wilcken, N. Wolmark, W. Wood, M. Zambetti, Increasing the dose intensity of chemotherapy by more frequent administration or sequential scheduling: a patient-level meta-analysis of 37298 women with early breast cancer in 26 randomised trials, Lancet 393 (10179) (2019) 1440–1452.
[5] J.Y. Ge, S. Shu, M. Kwon, B. Jovanovic, K. Murphy, A. Gulvady, A. Fassl, A. Trinh, Y. Kuang, G.A. Heavey, A. Luoma, C. Paweletz, A.R. Thorner, K.W. Wucherpfennig, J. Qi, M. Brown, P. Sicinski, T.O. McDonald, D. Pellman, F. Michor, K. Polyak, Acquired resistance to combined BET and CDK4/6 inhibition in triple-negative breast cancer, Nat. Commun. 11 (1) (2020) 2350.
[6] Y. Wu, X. Chen, S. Wang, S. Wang, Advances in the relationship between glycosyltransferases and multidrug resistance in cancer, Clin. Chim. Acta 495 (2019) 417–421.
[7] O. Saatci, A. Kaymak, U. Raza, P.G. Ersan, O. Akbulut, C.E. Banister, V. Sikirzhytski, U.M. Tokat, G. Aykut, S.A. Ansari, H.T. Dogan, M. Dogan, P. Jandaghi, A. Isik, F. Gundogdu, K. Kosemehmetoglu, O. Dizdar, S. Aksoy, A. Akyol, A. Uner, P.J. Buckhaults, Y. Riazalhosseini, O. Sahin, Targeting lysyl oxidase (LOX) overcomes chemotherapy resistance in triple negative breast cancer, Nat. Commun. 11 (1) (2020) 2416.
[8] J.P. Friedmann Angeli, D.V. Krysko, M. Conrad, Ferroptosis at the crossroads of cancer-acquired drug resistance and immune evasion, Nat. Rev. Cancer 19 (7) (2019) 405–414.
[9] N. Traverso, R. Ricciarelli, M. Nitti, B. Marengo, A.L. Furfaro, M.A. Pronzato, U. M. Marinari, C. Domenicotti, Role of glutathione in cancer progression and chemoresistance, Oxid. Med. Cell. Longev. 2013 (2013) 972913.
[10] I.G. Ryoo, B.H. Choi, S.K. Ku, M.K. Kwak, High CD44 expression mediates p62-associated NFE2L2/NRF2 activation in breast cancer stem cell-like cells: implications for cancer stem cell resistance, Redox Biol. 17 (2018) 246–258.
[11] E.Y. Park, E. Chang, E.J. Lee, H.W. Lee, H.G. Kang, K.H. Chun, Y.M. Woo, H. K. Kong, J.Y. Ko, H. Suzuki, E. Song, J.H. Park, Targeting of miR34a-NOTCH1 axis reduced breast cancer stemness and chemoresistance, Cancer Res. 74 (24) (2014) 7573–7582.
[12] A.M. Calcagno, C.D. Salcido, J.P. Gillet, C.P. Wu, J.M. Fostel, M.D. Mumau, M. M. Gottesman, L. Varticovski, S.V. Ambudkar, Prolonged drug selection of breast cancer cells and enrichment of cancer stem cell characteristics, J. Natl. Cancer Inst. 102 (21) (2010) 1637–1652.
[13] V.S. Viswanathan, M.J. Ryan, H.D. Dhruv, S. Gill, O.M. Eichhoff, B. Seashore-Ludlow, S.D. Kaffenberger, J.K. Eaton, K. Shimada, A.J. Aguirre, S.R. Viswanathan, S. Chattopadhyay, P. Tamayo, W.S. Yang, M.G. Rees, S. Chen, Z.V. Boskovic, S. Javaid, C. Huang, X. Wu, Y.Y. Tseng, E.M. Roider, D. Gao, J.M. Cleary, B. M. Wolpin, J.P. Mesirov, D.A. Haber, J.A. Engelman, J.S. Boehm, J.D. Kotz, C. S. Hon, Y. Chen, W.C. Hahn, M.P. Levesque, J.G. Doench, M.E. Berens, A.F. Shamji, P.A. Clemons, B.R. Stockwell, S.L. Schreiber, Dependency of a therapy-resistant state of cancer cells on a lipid peroxidase pathway, Nature 547 (7664) (2017) 453–457.
[14] D.L. Schonberg, T.E. Miller, Q. Wu, W.A. Flavahan, N.K. Das, J.S. Hale, C. G. Hubert, S.C. Mack, A.M. Jarrar, R.T. Karl, A.M. Rosager, A.M. Nixon, P.J. Tesar, P. Hamerlik, B.W. Kristensen, C. Horbinski, J.R. Connor, P.L. Fox, J.D. Lathia, J. N. Rich, Preferential iron trafficking characterizes glioblastoma stem-like cells, Cancer Cell 28 (4) (2015) 441–455.
[15] S.J. Dixon, K.M. Lemberg, M.R. Lamprecht, R. Skouta, E.M. Zaitsev, C.E. Gleason, D.N. Patel, A.J. Bauer, A.M. Cantley, W.S. Yang, B. Morrison 3rd, B.R. Stockwell, Ferroptosis: an iron-dependent form of nonapoptotic cell death, Cell 149 (5) (2012) 1060–1072.
[16] W.S. Yang, B.R. Stockwell, Ferroptosis: death by lipid peroxidation, Trends Cell Biol. 26 (3) (2016) 165–176.

[17] Z. Chen, J.J. Yin, Y.T. Zhou, Y. Zhang, L. Song, M. Song, S. Hu, N. Gu, Dual enzyme-like activities of iron oxide nanoparticles and their implication for diminishing cytotoxicity, ACS Nano 6 (5) (2012) 4001–4012.
[18] Y. Zhang, X. Fu, J. Jia, T. Wikerholmen, K. Xi, Y. Kong, J. Wang, H. Chen, Y. Ma, Z. Li, C. Wang, Q. Qi, F. Thorsen, J. Wang, J. Cui, X. Li, S. Ni, Glioblastoma therapy using codelivery of cisplatin and glutathione peroxidase targeting siRNA from iron oxide nanoparticles, ACS Appl. Mater. Interfaces 12 (39) (2020) 43408–43421.
[19] F. Zhang, F. Li, G.H. Lu, W. Nie, L. Zhang, Y. Lv, W. Bao, X. Gao, W. Wei, K. Pu, H. Y. Xie, Engineering magnetosomes for ferroptosis/immunomodulation synergism in cancer, ACS Nano 13 (5) (2019) 5662–5673.
[20] X. Xiang, H. Pang, T. Ma, F. Du, L. Li, J. Huang, L. Ma, L. Qiu, Ultrasound targeted microbubble destruction combined with Fe-MOF based bio-/enzyme-mimics nanoparticles for treating of cancer, J. Nanobiotechnol. 19 (1) (2021) 92.
[21] X.J. Yang, X.M. Xu, J. Xu, Y.F. Han, Iron oxychloride (FeOCl): an efficient Fenton-like catalyst for producing hydroxyl radicals in degradation of organic contaminants, J. Am. Chem. Soc. 135 (43) (2013) 16058–16061.
[22] W. Feng, X. Han, R. Wang, X. Gao, P. Hu, W. Yue, Y. Chen, J. Shi, Nanocatalysts-augmented and photothermal-enhanced tumor-specific sequential nanocatalytic therapy in both NIR-I and NIR-II biowindows, Adv. Mater. 31 (5) (2019) e1805919.
[23] Z. Tang, Y. Liu, M. He, W. Bu, Chemodynamic therapy: tumour microenvironment-mediated Fenton and Fenton-like reactions, Angew Chem. Int. Ed. Engl. 58 (4) (2019) 946–956.
[24] N.K. Das, A.J. Schwartz, G. Barthel, N. Inohara, Q. Liu, A. Sankar, D.R. Hill, X. Ma, O. Lamberg, M.K. Schnizlein, J.L. Arques, J.R. Spence, G. Nunez, A.D. Patterson, D. Sun, V.B. Young, Y.M. Shah, Microbial metabolite signaling is required for systemic iron homeostasis, Cell Metabol. 31 (1) (2020) 115–130.
[25] I. De Domenico, D.M. Ward, J. Kaplan, Specific iron chelators determine the route of ferritin degradation, Blood 114 (20) (2009) 4546–4551.
[26] P.K. Koochana, A. Mohanty, S. Das, B. Subhadarshanee, S. Satpati, A. Dixit, S. C. Sabat, R.K. Behera, Releasing iron from ferritin protein nanocage by reductive method: the role of electron transfer mediator, Biochim. Biophys. Acta Gen. Subj. 1862 (5) (2018) 1190–1198.
[27] A. La, T. Nguyen, K. Tran, E. Sauble, D. Tu, A. Gonzalez, T.Z. Kidane, C. Soriano, J. Morgan, M. Doan, K. Tran, C.Y. Wang, M.D. Knutson, M.C. Linder, Mobilization of iron from ferritin: new steps and details, Metallomics 10 (1) (2018) 154–168.
[28] R.C. Hider, X. Kong, Iron speciation in the cytosol: an overview, Dalton Trans. 42 (9) (2013) 3220–3229.
[29] R.K. Watt, R.J. Hilton, D.M. Graff, Oxido-reduction is not the only mechanism allowing ions to traverse the ferritin protein shell, Biochim. Biophys. Acta 1800 (8) (2010) 745–759.
[30] C. Badu-Boateng, R.J. Naftalin, Ascorbate and ferritin interactions: consequences for iron release in vitro and in vivo and implications for inflammation, Free Radic. Biol. Med. 133 (2019) 75–87.
[31] B. Jiang, X. Chen, G. Sun, X. Chen, Y. Yin, Y. Jin, Q. Mi, L. Ma, Y. Yang, X. Yan, K. Fan, A natural drug entry channel in the ferritin nanocage, Nano Today 35 (2020) 100948.
[32] C.Y. Lin, M.J. Shieh, Near-infrared fluorescent dye-decorated nanocages to form grenade-like nanoparticles with dual control release for photothermal theranostics and chemotherapy, Bioconjugate Chem. 29 (4) (2018) 1384–1398.
[33] R. Yang, J. Tian, Y. Liu, Z. Yang, D. Wu, Z. Zhou, Thermally induced encapsulation of food nutrients into phytoferritin through the flexible channels without additives, J. Agric. Food Chem. 65 (46) (2017) 9950–9955.
[34] L.N. Turino, M.R. Ruggiero, R. Stefania, J.C. Cutrin, S. Aime, S. Geninatti Crich, Ferritin decorated PLGA/paclitaxel loaded nanoparticles endowed with an enhanced toxicity toward MCF-7 breast tumor cells, Bioconjugate Chem. 28 (4) (2017) 1283–1290.
[35] T. Tan, H. Wang, H. Cao, L. Zeng, Y. Wang, Z. Wang, J. Wang, J. Li, S. Wang, Z. Zhang, Y. Li, Deep tumor-penetrated nanocages improve accessibility to cancer stem cells for photothermal-chemotherapy of breast cancer metastasis, Adv. Sci. 5 (12) (2018) 1801012.
[36] L. Conti, S. Lanzardo, R. Ruiu, M. Cadenazzi, F. Cavallo, S. Aime, S. Geninatti Crich, L-Ferritin targets breast cancer stem cells and delivers therapeutic and imaging agents, Oncotarget 7 (41) (2016) 66713–66727.
[37] B. Du, S. Jia, Q. Wang, X. Ding, Y. Liu, H. Yao, J. Zhou, A self-targeting, dual ROS/pH-Responsive apoferritin nanocage for spatiotemporally controlled drug delivery to breast cancer, Biomacromolecules 19 (3) (2018) 1026–1036.
[38] C.Y. Liu, C.J. Huang, Functionalization of polydopamine via the Aza-Michael reaction for antimicrobial interfaces, Langmuir 32 (19) (2016) 5019–5028.
[39] R. Zheng, S. Wang, Y. Tian, X. Jiang, D. Fu, S. Shen, W. Yang, Polydopamine-coated magnetic composite particles with an enhanced photothermal effect, ACS Appl. Mater. Interfaces 7 (29) (2015) 15876–15884.
[40] C. Du, X.J. Wu, M. He, Y.M. Zhang, R. Zhang, C.M. Dong, Polymeric photothermal agents for cancer therapy: recent progress and clinical potential, J. Mater. Chem. B 9 (6) (2021) 1478–1490.
[41] B. Li, T. Gong, N. Xu, F. Cui, B. Yuan, Q. Yuan, H. Sun, L. Wang, J. Liu, Improved stability and photothermal performance of polydopamine-modified Fe_3O_4 nanocomposites for highly efficient magnetic resonance imaging-guided photothermal therapy, Small 16 (45) (2020) e2003969.
[42] Y. Liu, K. Ai, J. Liu, M. Deng, Y. He, L. Lu, Dopamine-melanin colloidal nanospheres: an efficient near-infrared photothermal therapeutic agent for in vivo cancer therapy, Adv. Mater. 25 (9) (2013) 1353–1359.
[43] O. Mykhaylyk, Y.S. Antequera, D. Vlaskou, C. Plank, Generation of magnetic nonviral gene transfer agents and magnetofection in vitro, Nat. Protoc. 2 (10) (2007) 2391–2411.
[44] J. Friedrich, C. Seidel, R. Ebner, L.A. Kunz-Schughart, Spheroid-based drug screen: considerations and practical approach, Nat. Protoc. 4 (3) (2009) 309–324.
[45] A.J. van der Vlies, C.P. O'Neil, U. Hasegawa, N. Hammond, J.A. Hubbell, Synthesis of pyridyl disulfide-functionalized nanoparticles for conjugating thiol-containing small molecules, peptides, and proteins, Bioconjugate Chem. 21 (4) (2010) 653–662.
[46] S. Zhang, Y. Li, Z. Bao, N. Sun, S. Lin, Internal cavity amplification of shell-like ferritin regulated with the change of the secondary and tertiary structure induced by PEF technology, Int. J. Biol. Macromol. 182 (2021) 849–857.
[47] A. Ullrich, S. Horn, Structural investigations on differently sized monodisperse iron oxide nanoparticles synthesized by remineralization of apoferritin molecules, J. Nanoparticle Res. 15 (8) (2013).
[48] L. Wu, T. Li, D. Blom, J. Zhao, S. Ghoshroy, Q. Wang, Synthesis and electron microscopic analysis of the self-assembly of polymer and ferritin core-shell structures, Microsc. Res. Tech. 74 (7) (2011) 636–641.
[49] X.D. Yuan, X. Zhao, R. Xia, Z.G. Xie, Y. Lin, Z.H. Su, Photothermally responsive magnetic nanoparticles for nitric oxide release to combat *Staphylococcus aureus* biofilms, ACS Appl. Nano Mater. 5 (12) (2022) 18799–18810.
[50] J.P. Friedmann Angeli, M. Schneider, B. Proneth, Y.Y. Tyurina, V.A. Tyurin, V. J. Hammond, N. Herbach, M. Aichler, A. Walch, E. Eggenhofer, D. Basavarajappa, O. Radmark, S. Kobayashi, T. Seibt, H. Beck, F. Neff, I. Esposito, R. Wanke, H. Forster, O. Yefremova, M. Heinrichmeyer, G.W. Bornkamm, E.K. Geissler, S. B. Thomas, B.R. Stockwell, V.B. O'Donnell, V.E. Kagan, J.A. Schick, M. Conrad, Inactivation of the ferroptosis regulator GPX4 triggers acute renal failure in mice, Nat. Cell Biol. 16 (12) (2014) 1180–1191.
[51] W.S. Yang, R. SriRamaratnam, M.E. Welsch, K. Shimada, R. Skouta, V. S. Viswanathan, J.H. Cheah, P.A. Clemons, A.F. Shamji, C.B. Clish, L.M. Brown, A. W. Girotti, V.W. Cornish, S.L. Schreiber, B.R. Stockwell, Regulation of ferroptotic cancer cell death by GPX4, Cell 156 (1–2) (2014) 317–331.
[52] H.T. Yuan, J.B. Ma, W. Huang, P. Gong, F. Shi, X.L. Xu, C.J. Fu, X.X. Wang, Y. K. Wong, Y. Long, X. Sun, W.H. Li, Z.J. Li, J.G. Wang, Antitumor effects of a distinct sonodynamic nanosystem through enhanced induction of immunogenic cell death and ferroptosis with modulation of tumor microenvironment, JACS Au 3 (5) (2023) 1507–1520.
[53] P. Nagy, Kinetics and mechanisms of thiol-disulfide exchange covering direct substitution and thiol oxidation-mediated pathways, Antioxidants Redox Signal. 18 (13) (2013) 1623–1641.
[54] X. Meng, J. Deng, F. Liu, T. Guo, M. Liu, P. Dai, A. Fan, Z. Wang, Y. Zhao, Triggered all-active metal organic framework: ferroptosis Machinery contributes to the apoptotic photodynamic antitumor therapy, Nano Lett. 19 (11) (2019) 7866–7876.
[55] L.M. Bystrom, M.L. Guzman, S. Rivella, Iron and reactive oxygen species: friends or foes of cancer cells? Antioxidants Redox Signal. 20 (12) (2014) 1917–1924.
[56] Q. Chen, L. Liu, Y. Lu, X. Chen, Y. Zhang, W. Zhou, Q. Guo, C. Li, Y. Zhang, Y. Zhang, D. Liang, T. Sun, C. Jiang, Tumor microenvironment-triggered aggregated magnetic nanoparticles for reinforced image-guided immunogenic chemotherapy, Adv. Sci. 6 (6) (2019) 1802134.
[57] J. Nam, S. Son, L.J. Ochyl, R. Kuai, A. Schwendeman, J.J. Moon, Chemo-photothermal therapy combination elicits anti-tumor immunity against advanced metastatic cancer, Nat. Commun. 9 (1) (2018) 1074.
[58] Q. Chen, Y. Chen, W. Zhang, Q. Huang, M. Hu, D. Peng, C. Peng, L. Wang, W. Chen, Acidity and glutathione dual-responsive polydopamine-coated organic-inorganic Hybrid hollow mesoporous silica nanoparticles for controlled drug delivery, ChemMedChem 15 (20) (2020) 1940–1946.
[59] H. Li, Y. Jia, X. Feng, J. Li, Facile fabrication of robust polydopamine microcapsules for insulin delivery, J. Colloid Interface Sci. 487 (2017) 12–19.
[60] V. Bitonto, D. Alberti, R. Ruiu, S. Aime, S. Geninatti Crich, J.C. Cutrin, L-ferritin: a theranostic agent of natural origin for MRI visualization and treatment of breast cancer, J. Contr. Release 319 (2020) 300–310.
[61] X. Ren, Y. Chen, H. Peng, X. Fang, X. Zhang, Q. Chen, X. Wang, W. Yang, X. Sha, Blocking autophagic flux enhances iron oxide nanoparticle photothermal therapeutic efficiency in cancer treatment, ACS Appl. Mater. Interfaces 10 (33) (2018) 27701–27711.
[62] Q.Q. Guan, R.M. Guo, S.H. Huang, F. Zhang, J. Liu, Z.Y. Wang, X. Yang, X.T. Shuai, Z. Cao, Mesoporous polydopamine carrying sorafenib and SPIO nanoparticles for MRI-guided ferroptosis cancer therapy, J. Contr. Release 320 (2020) 392–403.
[63] S. Huang, B. Cao, J. Zhang, Y. Feng, L. Wang, X. Chen, H. Su, S. Liao, J. Liu, J. Yan, B. Liang, Induction of ferroptosis in human nasopharyngeal cancer cells by cucurbitacin B: molecular mechanism and therapeutic potential, Cell Death Dis. 12 (3) (2021) 237.
[64] F.T. Zeng, L.G. Tang, Q.Y. Zhang, C.R. Shi, Z.C. Huang, S.R.Y. Nijiati, X.Y. Chen, Z. J. Zhou, Coordinating the mechanisms of action of ferroptosis and the photothermal effect for cancer theranostics, Angew. Chem. Int. Ed. 61 (13) (2022) e202112925.
[65] H.T. Yuan, P. Xia, X. Sun, J.B. Ma, X.L. Xu, C.J. Fu, H.C. Zhou, Y.D. Guan, Z.F. Li, S. S. Zhao, H.F. Wang, L.Y. Dai, C.C. Xu, S.H. Dong, Q.S. Geng, Z.J. Li, J.G. Wang, Photothermal nanozymatic nanoparticles induce ferroptosis and apoptosis through tumor microenvironment manipulation for cancer therapy, Small 18 (41) (2022) e2202161.
[66] M. He, Y.Y. Song, W. Xu, X.L. Zhang, C.M. Dong, Four birds with one stone: a multifunctional polypeptide nanocomposite to unify ferroptosis, nitric oxide, and photothermia for amplifying antitumor immunity, Adv. Funct. Mater. 33 (40) (2023) 2304216.
[67] F. Ursini, M. Maiorino, Lipid peroxidation and ferroptosis: the role of GSH and GPX4, Free Radic. Biol. Med. 152 (2020) 175–185.
[68] Y. Liu, Z. Ye, W. Yang, Y. Hu, Y. Zhao, Z. Li, B. Xu, D. Chen, J. Tu, Y. Shen, A triple enhanced permeable gold nanoraspberry designed for positive feedback interventional therapy, J. Contr. Release 345 (2022) 120–137.

[69] I. Marangon, A.A. Silva, T. Guilbert, J. Kolosnjaj-Tabi, C. Marchiol, S. Natkhunarajah, F. Chamming's, C. Menard-Moyon, A. Bianco, J.L. Gennisson, G. Renault, F. Gazeau, Tumor stiffening, a Key determinant of tumor progression, is reversed by nanomaterial-induced photothermal therapy, Theranostics 7 (2) (2017) 329–343.

[70] L. Liu, Y. Wang, X. Guo, J. Zhao, S. Zhou, A biomimetic polymer magnetic nanocarrier polarizing tumor-associated macrophages for potentiating immunotherapy, Small 16 (38) (2020) e2003543.

[71] H. Zhao, B. Zhao, L. Wu, H. Xiao, K. Ding, C. Zheng, Q. Song, L. Sun, L. Wang, Z. Zhang, Amplified cancer immunotherapy of a surface-engineered antigenic microparticle vaccine by synergistically modulating tumor microenvironment, ACS Nano 13 (11) (2019) 12553–12566.

[72] D. Li, M. Zhang, F. Xu, Y. Chen, B. Chen, Y. Chang, H. Zhong, H. Jin, Y. Huang, Biomimetic albumin-modified gold nanorods for photothermo-chemotherapy and macrophage polarization modulation, Acta Pharm. Sin. B 8 (1) (2018) 74–84.